Evaluation of core beta effects on pedestal MHD stability in ITER and consequences for energy confinement

Oosterbeek, Wouter

Award date:
2018

Technische Universiteit Eindhoven University of Technology

Dual Master's
Science and Technology of Nuclear Fusion & Applied Physics (Plasma track)

Evaluation of core beta effects on pedestal MHD stability in ITER and consequences for energy confinement

Master thesis

Presentation and defence: July 20, 2018, 14:00h, Eindhoven

Wouter Oosterbeek

Supervisors

Daily supervisor:	dr.ir. T. Weyens
Science and Technology of Nuclear Fusion supervisor:	prof.dr.ir. G.T.A. Huijsmans
Applied Physics supervisor:	dr.ir. J. van Dijk
ITER supervisor:	dr.ir. A. Loarte

Graduation Committee members:

Science and Technology of Nuclear Fusion	**Applied Physics**
prof.dr.ir. G.T.A. Huijsmans	dr.ir. J. van Dijk
dr.ir. J. van Dijk	prof.dr.ir. G.T.A. Huijsmans
dr.ir. H.J. de Blank	dr.ir. A.J.M. Mackus
prof.dr.ir. M.R. de Baar	dr.ir. M. Duran Matute

Eindhoven, July 13, 2018

Abstract

Nuclear fusion is one of the great promises as a source of energy for the future. Magnetic confinement fusion, in which a hot plasma is confined by magnetic fields, is now nearing the point at which more energy is produced by fusion reactions in the plasma than is put in. This (temporary) net fusion power gain, is the goal for ITER, the newest fusion reactor that is still under construction in the south of France. This is also the place where the research is conducted for this Master's graduation project. In order to reach the goal of a positive energy balance, a certain configuration of the plasma, called high confinement mode (H-mode), is essential. In this H-mode, which was discovered in the 1980's and of which the details of the physics are still not exactly known, there is a high pressure gradient at the edge of the plasma, also referred to as the pedestal. This increases the stored plasma energy significantly and causes the increase of the energy confinement time by a factor two.

The height of the pedestal (the pressure at the top of the pedestal) is thus an interesting parameter and it is known that it is increased by increasing the core pressure, through an MHD effect called Shafranov shift. On top of that, the height of the pedestal also has a beneficial effect on the core pressure through stiffness of the pressure profile, resulting in a positive feedback mechanism. This is researched for other devices, but since a saturation limit for high β_N was found in [1], consequences for ITER regarding this feedback mechanism are not known.

A comprehensive model was created using the ideal MHD equilibrium code HELENA to calculate 2D equilibria and the ideal MHD stability code MISHKA to calculate stability of these equilibria. HELENA was adapted so that core and edge pressure can be changed separately. Using this, a parameter scan over $\beta_{p,ped}, \beta_N$ for a range of different toroidal mode numbers is done and a relation between maximum achievable pedestal height and total pressure is found.

Simulations are done for three different ITER scenarios: 15MA/5.3T (Q=10 scenario), 10MA/5.3T (steady-state scenario) and 7.5MA/2.65T (Half field-half current scenario). For the 15MA and 7.5MA scenarios, no saturation limit was found, but it was seen that a pedestal width that scales as $\Delta_\psi \propto \beta_{p,ped}^{1/2}$ gives a larger increase of the maximum attainable pedestal height as function of β_N. A difference is seen comparing those to the 10MA scenario. A large region in the researched parameter space was found to be limited by $n = 2$ kink-peeling modes, most likely due to a reverse in shear near the edge, which stabilizes high-n modes. This region causes a plateau, a range of β_N values over which $\beta_{p,ped}$ is constant. This is not a saturation limit, but since ITER operation is mostly in this range, it can have consequences for operation in this scenario.

For the two inductive scenarios (15MA, 7.5MA), a power law relation gives a good fit for the data. A comparison to experimental values from JET [2] give ballpark the same value as found for the simulations in which the pedestal width is varied, for the experiment that resembles ITER conditions most. The steady-state scenario (10MA) does not agree with the power law relation, so that comparison is more difficult.

When assuming values of the profile stiffness, consequences for energy confinement can be looked at. For the same scaling as considered in the IPB98(y,2) ITER

scaling law [3], a stiffness of $\delta = 0.263$ is necessary and in order to have a stable (controllable) burning plasma the stiffness is limited to $\delta \leq 0.424$. However, since values for profile stiffness cannot be obtained from other devices, ITER experiments will have to show how confinement is actually influenced.

Contents

1 Introduction **1**
2 Theory **7**
2.1 Ideal MHD 7
2.2 Equilibrium and stability 9
2.2.1 Energy Principle 10
2.2.2 MHD instabilities: a description of different modes 11
2.2.3 HELENA 14
2.2.4 MISHKA 14
2.3 Core pressure effects on MHD pedestal stability 15
2.4 ITER confinement and scaling law comparison 17
3 Numerical method **19**
3.1 HELENA parameters 19
3.2 MISHKA parameters 22
3.3 A look at different ITER scenarios 22
3.3.1 Q=10 scenario: 15MA-5.3T 24
3.3.2 Half field-Half current scenario: 7.5MA-2.65T 24
3.3.3 Q=5 steady-state scenario: 10MA-2.65T 24
4 Results and discussion **27**
4.1 15MA-5.3T constant pedestal width 27
4.2 7.5MA-2.65T constant pedestal width 30
4.3 10MA-5.3T constant pedestal width 32
4.4 Varying pedestal width 35
4.5 Derivation of a relation between pedestal and total pressure from MHD stability graphs 37
4.6 Comparison to scaling law 39
5 Conclusions and future work **41**
List of Figures **43**
List of Tables **43**
Bibliography **45**
A Additional graphs **49**
A.1 Mode structures 49
A.1.1 15MA-5.3T 50
A.1.2 7.5MA-2.65T 51
A.1.3 10MA-5.3T 52
A.2 Non-normalized current density and pressure profiles 53
B EPS conference **54**
B.1 Poster 54
B.2 four page paper 56
C Input files **61**
C.1 HELENA input file example 61
C.2 MISHKA input file example 62

Chapter 1

Introduction

The way energy is consumed nowadays is causing one of the major problems humanity is dealing with right now. This problem, sometimes referred to as the energy problem, actually has two separate aspects. First of all, the effects of the cumulative emission of huge amounts of greenhouse gases (due to fossil fuels) are known to be harmful for earth's environment, and secondly, we are running out of the finite supply of these fossil fuels, according to estimates within fifty years [4], especially with the growing demand for energy. Therefore, new sources of energy are needed.

Quite a few of these alternative energy sources are already being developed, but for most of them there are some fundamental limits. For example, solar energy and wind energy are limited through their intermittency and low energy density, whereas others like geothermal energy and hydro power energy require to be located in a suitable geological setting. On the other hand, there is also nuclear fission, which has to cope with other problems: radioactive waste, weapon proliferation and catastrophic nuclear meltdowns. On top of that, the problem of having a finite amount of available fuel is also applicable to uranium. There are even more options for alternative energy sources, but they all have their problems. One of the most promising amongst them, however, is nuclear fusion, which could be a great source for base load energy supply. [5, Chapter 2]

The problem with nuclear fusion is the enormous difficulty to obtain energy from it on earth. The idea has been around since the 1950's and research is still being conducted in order to achieve a positive energy balance (getting more energy out than putting in). However, it has great potential benefits, since it is a clean form of energy that is not location or weather dependent, produces only minimal radioactive waste, without possibility of meltdown-like events or weapon proliferation and with enough fuel (consisting of hydrogen isotopes deuterium and tritium) available to supply energy for at least thousands of years [5, p53], with other estimates that go up to as far as six million years [6].

Nuclear fusion is the process that occurs in the sun: energy is released when small atoms fuse their cores together to form bigger ones. The difference in binding energy (per nucleon) is released when this reaction occurs. This can only happen when electrons are separated from the core of the atoms. Heating atoms beyond the solid, liquid and gaseous phases results in the formation of a plasma. This plasma, also referred to as the fourth state of matter, is a macroscopically neutral ionized gas, which contains electrons and ions (and in general often also still neutral particles). This plasma has to be confined in some way to obtain nuclear fusion. The sun uses

its own gravity for that, but on earth another solution has to be found.

Different kinds of devices and techniques of confinement are currently researched, but since the research conducted for this graduation project is done at the fusion reactor under construction called ITER, this device will be taken as example and will be explained in more detail. Taking advantage of the charge of the particles in the plasma, it can be confined by magnetic fields. ITER is such a magnetic confinement fusion device. More precisely, it is a tokamak: an axisymmetric, toroidal (donut-shaped) device, firstly designed in the late 1950s at the Kurchatov Institute in Moscow [7].

The idea for ITER (Latin for 'the way' and an acronym for 'International Thermonuclear Experimental Reactor') already originated in 1985 and is being built as a collaboration of 35 nations. It is planned to be the first fusion energy device in which more power is produced through nuclear fusion than is put in the plasma by various means of heating, thus showing that controlled fusion works as a source of energy on earth. Since then, great discoveries were already made at other fusion reactors. One of these is the so-called high confinement mode (H-mode), which was discovered in 1982 at the Max Planck Institute for Plasma Physics (IPP) in Garching, Germany. An example of a typical H-mode pressure profile is schematically given in figure 1.1, in which the pedestal is given by the grey area. A strong pressure gradient at the edge of the plasma (also referred to as the pedestal) arises when sufficient heating power is applied, as a result of stabilization of turbulence in a region at the edge of the plasma. The transport then decreases which leads to a strong pressure gradient. In H-mode the pressure gradient is typically no longer limited by transport, but by instabilities calculated through a theory called MagnetoHydroDynamics (MHD), which is a theory in which the plasma is seen as a conducting fluid moving in a magnetic field. It is mathematically derived from a combination of the kinetic theory (by Boltzmann and Vlasov) and the Maxwell equations. The emergence of a pedestal results in a better confinement of the plasma compared to a configuration in which the pressure gradient does not exist. Confinement is measured through the energy confinement time (τ_E), mathematically defined as $\tau_E = \frac{W_p}{P - dW_p/dt}$ with W_p the total energy stored in the plasma and P the total heating power. This energy confinement time basically says how long it takes for energy to escape the plasma (and if this is longer, the confinement is better so that more fusion reactions can occur). Through H-mode τ_E is improved roughly by a factor two. Although the exact physics details of the stabilization of turbulence are not completely understood yet (there are theories), attaining the H-mode configuration is of major importance for ITER. [8]

In figure 1.2 the distinction between edge and core is schematically depicted in a poloidal cross section of a tokamak. Also, the so-called separatrix is shown, which is the transition between closed and open flux surfaces, and the X-point in which the magnetic field is purely toroidal. The scrape-off layer (SOL) is the region outside of the separatrix in which the particles are guided to the divertor region, where energy is subtracted from the plasma. The edge is defined slightly differently in this project, only taking the region in which closed flux surfaces are still present, up to but not including the separatrix. This is done because of numerical reasons.

However, there are also still challenges to overcome before ITER can produce energy. One of these are the so-called Edge-Localized Modes (ELMs), which are periodic outbursts of plasma that occur in H-mode plasmas, comparable (at least

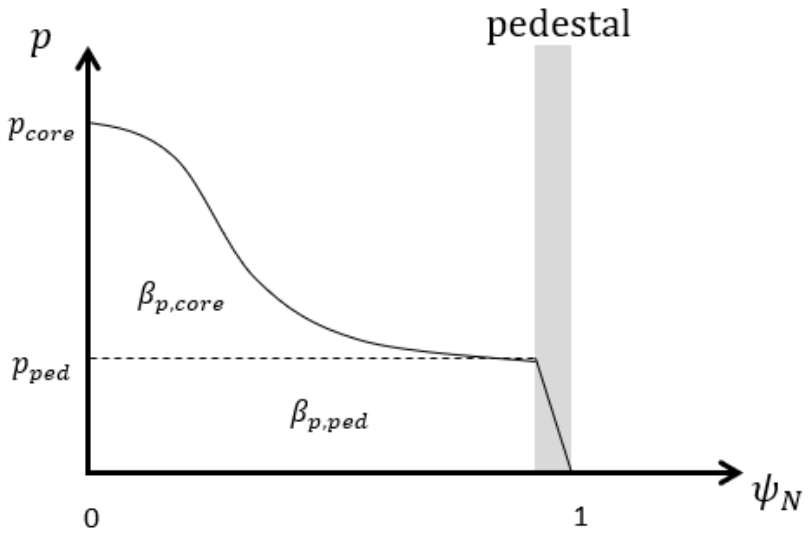

Figure 1.1: Example of a pressure profile for H-mode fusion plasmas, with the pedestal depicted in the region of high normalized poloidal magnetic flux ψ (a radial coordinate with $\psi_N = 0$ in the core of the plasma, $\psi_N = 1$ at the edge). β_p is the ratio between kinetic pressure (integrated pressure) and poloidal magnetic field pressure, which for reasons discussed later (section 2.3) is split in a pedestal part, $\beta_{p,ped}$ and a core part, $\beta_{p,core}$.

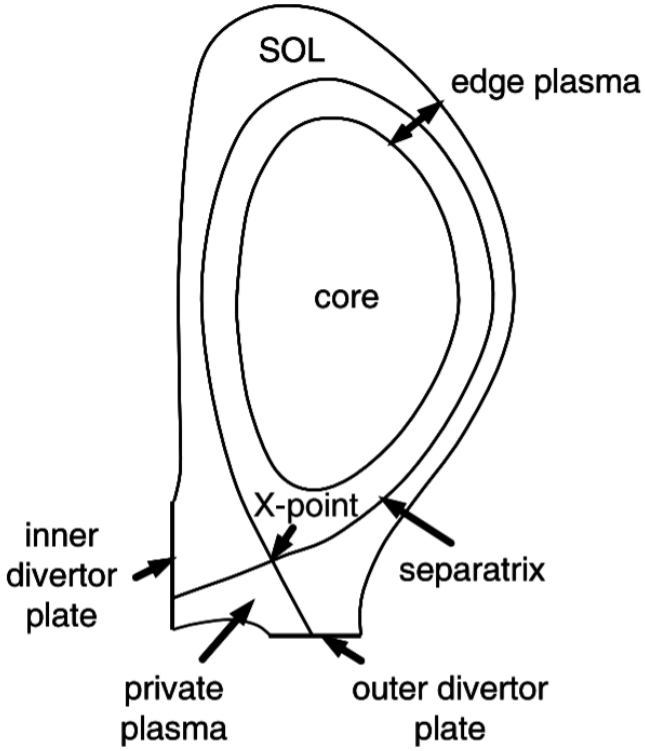

Figure 1.2: A poloidal cross section of a tokamak. Important for this project is the distinction between core and edge regions, although in this research the edge region is only up to the separatrix, which is the at the transition of closed flux surfaces to open field lines. Also of importance is the X-point, at which the magnetic field is purely toroidal. Figure taken from [9, figure 1].

in morphology) to solar flares from the sun [10]. ELMs result in higher heat loads through which eventually the wall can be damaged, although they can also be beneficial e.g. in impurity removal. [11] The dynamics of these ELMs can be described through the aforementioned MHD theory. From this perspective, it is stated that ELMs are the result of MHD instabilities at the edge of the plasma that happen as a consequence of the high pressure gradient and resulting bootstrap current in the pedestal region.

This is a current that is caused by some fraction of the particles that don't have enough energy to overcome the higher magnetic field close to the center of the torus (a so-called neoclassical effect: an effect due to the three-dimensional shape of the torus). These particles don't completely move around but are trapped in trajectories that are called banana orbits (due to their shape) and in combination with a pressure gradient this leads to an extra current, self-induced by the plasma, with the name bootstrap current. On top of that, in general, a pressure gradient causes a large current especially at the outboard side of the tokamak, also for particles that aren't trapped, which can be seen through the R^2 dependence, with R the radial distance from the center of the tokamak, from equation (2.24). Altogether, this leads to a peak in the current density profile at the edge of the plasma, but especially at the outboard side of the tokamak. The corresponding destabilized MHD modes that are seen when ELMs occur are the ballooning modes (driven by pressure gradients) and peeling modes (driven by edge currents parallel to the magnetic field) or the coupled peeling-ballooning modes. These are the main candidate of the theory behind ELMs. [12]

In this Master's graduation project the relation between MHD stability at the edge of the plasma and the core pressure will be looked at through numerical codes. The stable maximum achievable height of the pedestal is larger for higher core pressures (because of MHD). On the other hand, there is also a transport effect, called profile stiffness. This is the relation between core and edge pressure, mainly determined by pressure gradients at every part of the profile. Profile stiffness causes the core pressure to increase when the pedestal height increases. Combining both effects leads to a positive feedback mechanism, in which the core and edge of the plasma influence each other. This feedback mechanism can be benefited from by heating the plasma, so that core pressure increases and the feedback mechanism occurs.

However, a saturation of this effect has been found in [1], as can be seen in figure 1.3. Here you see the pressure at the top of the pedestal as a function of $\beta_N = \beta_t \frac{aB_t}{\mu_0 I_p} = \frac{<p>}{B_t^2/2\mu_0} \frac{aB_t}{\mu_0 I_p}$ with $< p >$ the volume integrated pressure, a the minor radius, B_t the toroidal magnetic field, μ_0 vacuum permeability and I_p the plasma current. So β_N is a normalized quantity that gives a measure of the total pressure. It is shown that a saturation limit is found in which $p_{ped,top}$, the pressure at the top of the pedestal, does not increase anymore with β_N. Results are given for two different parameters that can be of influence to fusion plasmas. Firstly, it is looked at for low and high triangularity, a parameter regarding the shape of the plasma defined as $triangularity = \frac{R_{ga} - R_{up}}{a}$ with R_{ga} and R_{up} the distance from the center of the tokamak to respectively the geometrical axis and the upper most vertical point of the last closed flux surface. A lower triangularity is shown to give a lower pedestal top pressure and a saturation limit for smaller β_N. Secondly, effective charges are looked at, which are defined as $Z_{\text{eff}} = \frac{\sum n_i Z_i^2}{\sum n_i Z_i}$ giving a measure for the amount of impurities

in the plasma. $Z_{\text{eff}} = 1.3$ (solid lines) and $Z_{\text{eff}} = 2.0$ (dashed lines) are compared. These don't differ very much although the saturation limit gives a slightly higher top pedestal pressure and, in the low triangularity case it saturates for slightly larger β_N. These are results from simulations with ideal MHD stability code MISHKA, used to calculate the maximum stable pedestal height. Unfortunately, it is not clear what kind of instabilities are dealt with here.

On top of the simulations, this core-edge feedback mechanism is also researched experimentally. An example of research into this is e.g. [2] at JET, results of which are given in figure 1.4. Here pedestal, core and total energy (volume integral of pressure) are looked at separately as function of heating power (directed at the core). It is seen that all increase, with the core increasing faster than the edge. Also, three different experiments were done: one with a carbon wall (C-wall) with a high triangularity plasma, and two with an ITER-like wall (ILW: Beryllium with Tungsten divertor), for both low and high triangularity. Note that, as with most results for current fusion devices, extrapolation to ITER is uncertain because of size and other conditions, such as the foreseen relatively large bootstrap current in ITER compared to current devices. Also note that the high-triangularity C-wall case is expected to be correspond best to ITER scenarios, because little gas puffing was needed, so that colliosionality (ratio of the electron-ion collision frequency to the banana orbit frequency) is low, so that edge bootstrap current is high, which is also the case for ITER.

Of course, because of the impact on energy confinement of the pedestal, these findings raise the question what this feedback mechanism will mean for ITER operation and if there is a saturation limit for ITER. In order to investigate this effect for ITER, a research question has been established:

> Can a comprehensive computational model be obtained by coupling MHD equilibrium code HELENA and stability code MISHKA, in order to see to which extent the feedback mechanism between core pressure and pedestal stability can be beneficiary for plasma confinement in ITER?

This research has been conducted at ITER Organization, under daily supervision of Toon Weyens (developer of PB3D, a 3D edge stability code which is still under development). This project will also be supervised by Guido Huijsmans, expert in MHD (in fusion) and (co-)developer of HELENA and MISHKA, Alberto Loarte, expert in modeling in the field of nuclear fusion and by Jan van Dijk, expert on numerical simulations for plasmas more generally (mainly through the Plasimo code).

The work done in this Master's graduation project was also presented at the European Physical Society (EPS) 45th conference on Plasma Physics, through a poster on july 3rd, 2018. The poster and accompanying four-page paper are given in Appendix B.

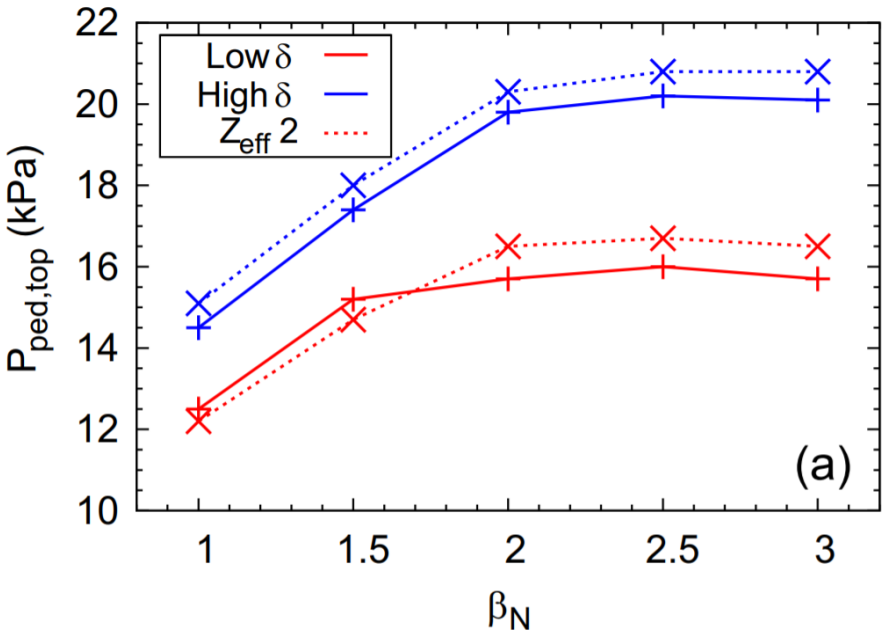

Figure 1.3: Figure, taken from [1, figure 1], of pedestal height as function of β_N, for both low and high triangularity and for two Z_{eff} values. It clearly shows a saturation limit at high β_N of the pedestal height.

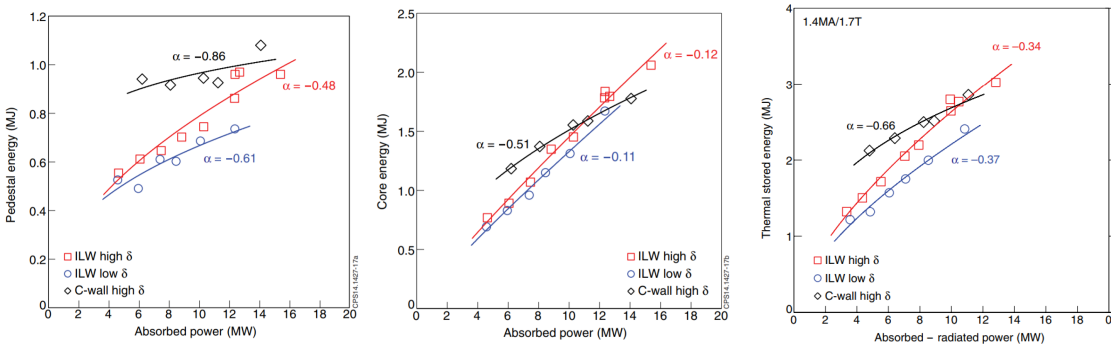

(a) Pedestal energy as function of absorbed power.

(b) Core energy as function of absorbed power.

(c) Total energy as a function of absorbed minus radiated power.

Figure 1.4: Pedestal, core and total energy separately as function of heating power. Note that in (c) the plotted absorbed-radiated power is slightly different than the absorbed power that is plotted in the other two graphs. It is looked at for a Carbon wall with a high triangularity plasma, and two experiments with an ITER-like wall, for both low and high triangularity. These graphs are taken from [2, Figures 16 and 17].

Chapter 2

Theory

In ITER, and other tokamaks, magnetic fields are used to create a magnetic pressure that counteracts the outward kinetic pressure of the plasma. There are several theories that describe this interaction between magnetic field and plasma , but the theory on which the research in this graduation project is based is Magnetohydrodynamics (MHD). MHD is the description of a conducting fluid moving within a magnetic field [13, p1].

The starting equations on which MHD was built were already well-known, when in the late 1930s astrophysicists realized that plasmas interacting with magnetic fields occur very commonly in space and MHD is a valuable theory to describe this. In engineering, MHD wasn't broadly used until the 1960s, in which the main application is for liquid metals in the metallurgical industries. Plasma physicists have been interested in MHD since the 1950s. For a great part this was a result of the rise of fusion energy research, but it is also used considering laboratory plasmas. Since its emergence, valuable theorems have been developed around the MHD theory, of which the 'energy principle' (see section 2.2.1) is an example. [13, paragraph 1.2]

In this chapter the MHD theory, or more precisely ideal MHD theory, will be described. Then it will be shown how this can be used to calculate equilibria and stability, which is what MHD is used for in the case of fusion plasmas. The aforementioned energy principle and how it is used in order to calculate this stability will be explained.

2.1 Ideal MHD

The theory of MHD considers a conducting fluid (Navier Stokes equations) in a magnetic field (Maxwell Equations). For the ideal MHD theory an extra assumption is made: the fluid is perfectly conducting. For fusion plasmas this is a valid approximation, considering the plasma resistivity gets very low at the high temperatures that are dealt with in fusion plasmas. Having a look at the full derivation of these ideal MHD equations is recommended (described in many books, for example by Freidberg [14, chapter 2]), but it is outside the scope of this report. The derivation starts from the Boltzmann equation, taking a statistical distribution function to describe a particle model in 6D phase-space (three spatial and three velocity dimensions), macroscopic quantities can be derived by calculating mathematical moments of this distribution function. This results in a two-fluid model. A low-frequency, short-wavelength approximation and additionally neglecting electron inertia leads

to the single fluid description. The low frequency Maxwell's equations are then also added and in order to close the system, assumptions about time and length scales are made. This results in the MHD theory, in which resistivity can be neglected (ideal Ohm's law) to obtain ideal MHD. This mathematical derivation, that is often quite tedious and in some cases requires subtle but clever thinking (according to Freidberg), ultimately leads to the following equations:

$$\frac{\partial \rho}{\partial t} + \nabla \cdot \rho \boldsymbol{v} = 0 \tag{2.1}$$

$$\rho \frac{d\boldsymbol{v}}{dt} = \boldsymbol{J} \times \boldsymbol{B} - \nabla p \tag{2.2}$$

$$\frac{d}{dt}\left(\frac{p}{\rho^\gamma}\right) = 0 \tag{2.3}$$

$$\boldsymbol{E} + \boldsymbol{v} \times \boldsymbol{B} = 0 \tag{2.4}$$

$$\nabla \times \boldsymbol{E} = -\frac{\partial \boldsymbol{B}}{\partial t} \tag{2.5}$$

$$\nabla \times \boldsymbol{B} = \mu_0 \boldsymbol{J} \tag{2.6}$$

$$\nabla \cdot \boldsymbol{B} = 0 \tag{2.7}$$

In these equations, ρ is the density, t the time, $\boldsymbol{v}$ the average velocity, p the pressure, $\boldsymbol{J}$ the current density, $\boldsymbol{B}$ the magnetic field, $\boldsymbol{E}$ the electric field, γ the ratio of specific heats and μ_0 the vacuum permeability. Also, $\frac{d}{dt} \equiv \frac{\partial}{\partial t} + \boldsymbol{v} \cdot \nabla$ represents the convective derivative. [14, chapter 2] These equations can separately be recognized by their physical meaning: (2.1) is the continuity equation (conservation of mass), (2.2) the conservation of momentum, (2.3) the conservation of (adiabatic) energy, (2.4) Ohm's law (ideal), (2.5) Faraday's equation, (2.6) Ampère's law and (2.7) is the divergence constraint on magnetic fields [15].

The derivation of these equations is achieved using three assumptions that limit the validity of ideal MHD:

$$\begin{aligned} &\text{High collisionality:} && \left(\frac{m_i}{m_e}\right)^{1/2} \frac{v_{th,i}\tau_{ii}}{a} \ll 1 \\ &\text{Small gyro radius:} && \frac{r_{L,i}}{a} \ll 1 \\ &\text{Small resistivity:} && \left(\frac{m_e}{m_i}\right)^{1/2} \frac{r_{L,i}^2}{a v_{th,i}\tau_{ii}} \ll 1 \end{aligned} \tag{2.8}$$

in which m_e and m_i represent the electron and ion mass, $v_{th,i}$ the ion thermal velocity, τ_{ii} the ion-ion collision time, a the minor radius of the plasma and $r_{L,i}$ the ion Larmor radius. In practice, these criteria mean that ideal MHD is valid for relatively large length (compared to the mean free path and gyro radius) and time (compared to the collision times) scales. [14]

Because of these assumptions, ideal MHD is a mathematically relatively comprehensive theory, with a region of validity that is, compared to other more general theories (e.g. a description of the plasma in 6D phase space with multiple ion species), quite narrow. When the three assumptions are compared with the conditions of fusion, it even shows the 'issue' that theoretically ideal MHD is not valid for

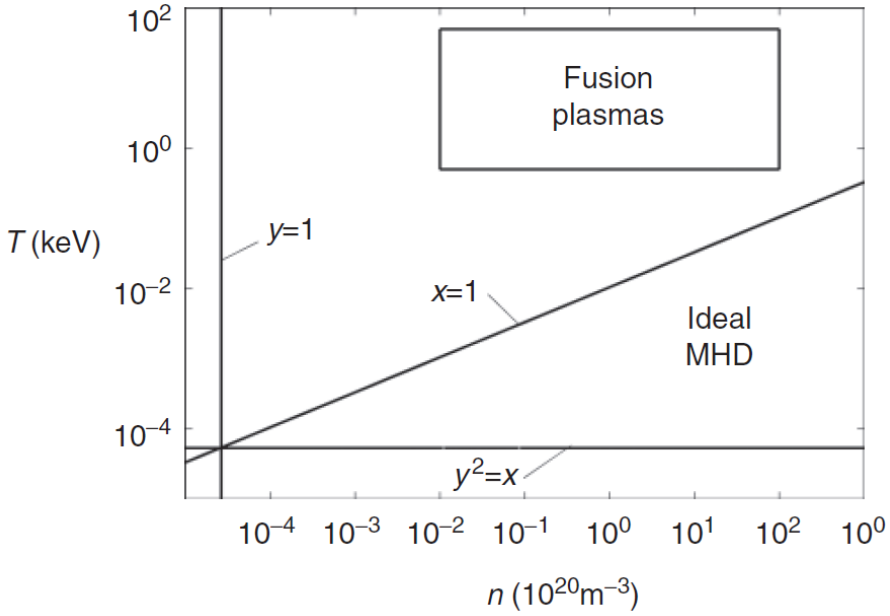

Figure 2.1: Validity of ideal MHD in density versus temperature parameter space, for $\beta = 0.05$ and a =1 m. Dimensionless variables $x = \left(\frac{m_i}{m_e}\right)^{1/2} \frac{v_{th,i}\tau_{ii}}{a}$ and $y = \frac{r_{L,i}}{a}$ show the three assumptions made for ideal MHD. The theoretical region of validity of MHD and the region of (n, T) values applicable to fusion are shown, which, as can be seen, theoretically don't overlap. [14, p30]

fusion plasmas, as shown in figure 2.1. The assumptions of small gyro radius and small resistivity are satisfied for fusion plasmas, but technically the high collisionality assumption does not apply to fusion plasmas. In practice, however, the magnetic field takes on the role that collisions play, which leads to strong anisotropy, i.e. behavior parallel and perpendicular to the magnetic field is very different, introduced by the magnetic field in toroidal configurations. As a consequence, ideal MHD can at least be used for the physics perpendicular to the magnetic field, whereas in the direction parallel to the magnetic field, ideal MHD, in particular equation (2.3), is almost always invalid. In that case, one has to resort to more general theories. For many research questions, though, including the one that is dealt with in this report, the main interest lies in the behavior of the plasma perpendicular to the magnetic field lines (in that direction, particles and energy escape from the plasma) so that this is not an issue. Finally it should be mentioned that at the very edge of the plasma, MHD is often also not valid, and the full dynamics of the plasma must be taken into account. In that case, more advanced models are needed. However, this is outside the scope of this project, which only uses ideal MHD. [16]

2.2 Equilibrium and stability

The purpose for which ideal MHD is used in this graduation project, is to look at the stability of the plasma. However, in order to check whether a plasma configuration is stable, the equilibrium needs to be calculated first. An equilibrium is a situation in which the plasma parameters don't change in time. Perturbing this situation slightly, stability can be checked. As depicted schematically in figure 2.2, it is stable when the

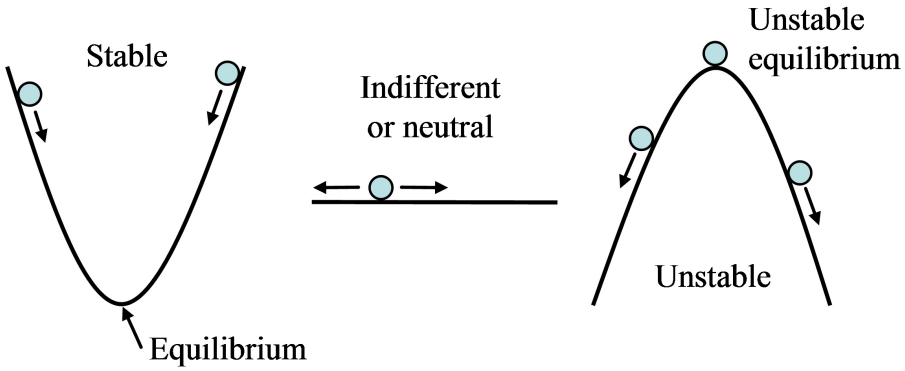

Figure 2.2: Schematic drawing of a stable, neutral and unstable equilibrium.[17]

perturbed plasma is driven back to the equilibrium situation by the forces that act upon the plasma and unstable when the plasma is driven away from its equilibrium by those MHD forces. These forces are described by the MHD equations; ultimately these will be given later in equation (2.13). For equilibria, there is also the indifferent case which lies in between the stable and unstable situation, which is called marginal stability. When longer periods of time are considered, going deeper into this matter one could also look at non-linear stability (taking higher order effects into account) but this is outside the scope of this report, which deals with linear stability only.

2.2.1 Energy Principle

One of the powerful theorems developed from (ideal) MHD is the Energy Principle. The mathematics start by linearizing the ideal MHD equations (2.1)-(2.7) as $Q(\boldsymbol{r},t) = Q_0 + Q_1$, with Q_0 the equilibrium quantity and Q_1 the perturbation of that quantity, taking $\boldsymbol{v_0} = 0$ and defining $\boldsymbol{v_1} \equiv \frac{\partial \boldsymbol{\xi}}{\partial t}$ (letting $\boldsymbol{\xi}$ be the displacement of the plasma: $\boldsymbol{r} = \boldsymbol{r_0} + \boldsymbol{\xi}$). By then taking the situation at $t = 0$ as the equilibrium (all perturbation quantities zero) with only a small velocity $\boldsymbol{v_1}(\boldsymbol{r_0}, 0) > 0$, the linearized equations are then solved, which gives equations of ρ_1, p_1 and $\boldsymbol{B_1}$ as a function of $\boldsymbol{\xi}(\boldsymbol{r_0}, t)$. A normal mode expansion is then used: $Q(\boldsymbol{r},t) = \widetilde{Q}(\boldsymbol{r})e^{-i\omega t}$. Using this, the perturbed quantities can be described as functions of the perturbed position and equilibrium quantities:

$$\rho_1 = -\nabla \cdot (\rho_0 \boldsymbol{\xi}) \tag{2.9}$$

$$p_1 = -\boldsymbol{\xi} \cdot \nabla p_0 - \gamma p_0 \nabla \cdot \boldsymbol{\xi} \tag{2.10}$$

$$\boldsymbol{B_1} = \nabla \times (\boldsymbol{\xi} \times \boldsymbol{B_0}) \tag{2.11}$$

Then, approximating products of perturbed quantities as zero and using equation (2.6) with $\boldsymbol{J_0} \times \boldsymbol{B_0} = \nabla p_0$ from the static equilibrium and plugging these into the linearized momentum equation (linearization of (2.2)) one gets:

$$\boldsymbol{F(\xi)} = \rho_0 \frac{\partial^2 \xi}{\partial t^2} = -\rho_0 \omega^2 \boldsymbol{\xi} \tag{2.12}$$

with

$$\boldsymbol{F(\xi)} = \frac{1}{\mu_0}(\nabla \times \boldsymbol{B_0}) \times \boldsymbol{B_1} + \frac{1}{\mu_0}(\nabla \times \boldsymbol{B_1}) \times \boldsymbol{B_0} - \nabla p_1 \tag{2.13}$$

the Force operator, which owes its name to the similarity with the $F = ma$ formula. With the equations for the perturbed quantities (2.9) - (2.11), it can be seen that it is only dependent on $\boldsymbol{\xi}$ (and equilibrium quantities and constants of nature).

The variational principle [18] can then be used for the stability problem, as is justified by the hermiticity of the force operator, so that the kinetic energy term for the linearized energy can be represented by $K \equiv \frac{1}{2}\int \rho \boldsymbol{\xi}^* \boldsymbol{\xi} dV$ and the perturbed potential energy by $\delta W \equiv -\frac{1}{2}\int \boldsymbol{\xi}^* \cdot \boldsymbol{F}(\boldsymbol{\xi}) dV$. The Rayleigh quotiënt can then be defined as the ratio of the potential and the kinetic energy and the stationary values can be shown to be equal to the complex normal mode frequency squared [19]:

$$\Lambda_{stat} = \left(\frac{\delta W}{K}\right)_{stat} = \omega^2. \tag{2.14}$$

The energy principle states that a sufficient and necessary condition for stability is:

$$\delta W(\boldsymbol{\xi}^*, \boldsymbol{\xi}) \geq 0, \tag{2.15}$$

which gives rise to a way of calculating stability. [14, chapter 8]

Extending the model to include a vacuum region surrounding the plasma, the perturbed potential energy can be written as a sum of the fluid energy (plasma potential energy), the surface energy and the vacuum energy: $\delta W = \delta W_F + \delta W_S + \delta W_V$. These can, as in [20], be written as:

$$\delta W_p(\boldsymbol{\xi}, \overline{\boldsymbol{Q}}) = \frac{1}{2}\int_{plasma} \left[\frac{|\overline{\boldsymbol{Q}}|^2}{\mu_0} + \gamma p |\nabla \cdot \boldsymbol{\xi}|^2 - 2(\boldsymbol{\xi} \cdot \nabla p)(\boldsymbol{\kappa} \cdot \boldsymbol{\xi}^*) - \sigma(\boldsymbol{\xi}^* \times \boldsymbol{B}) \cdot \overline{\boldsymbol{Q}}\right] dV, \tag{2.16}$$

$$\delta W_s(\boldsymbol{\xi}_{\boldsymbol{n}}) = \frac{1}{2}\int_{surface} \left[|\boldsymbol{n} \cdot \boldsymbol{\xi}|^2 \boldsymbol{n} \cdot \left[\!\left[\nabla\left(\mu_0 p + \frac{B^2}{2}\right)\right]\!\right]\right] dS \tag{2.17}$$

and

$$\delta W_v(\boldsymbol{Q}_{\boldsymbol{v}}) = \frac{1}{2}\int_{vacuum} \frac{|\boldsymbol{Q}_{\boldsymbol{v}}|^2}{\mu_0} dV, \tag{2.18}$$

with $\boldsymbol{Q} \equiv \boldsymbol{B_1} = \nabla \times (\boldsymbol{\xi} \times \boldsymbol{B_0})$ the perturbation of the magnetic field, $\overline{\boldsymbol{Q}}$ defined as $\overline{\boldsymbol{Q}} \equiv \boldsymbol{Q} - \boldsymbol{B}\frac{\mu_0 \boldsymbol{\xi} \cdot \nabla p}{B^2} = \boldsymbol{Q}_\perp - \boldsymbol{B}(\nabla \cdot \boldsymbol{\xi}_\perp + 2\boldsymbol{\xi}_\perp \cdot \boldsymbol{\kappa})$, γ the adiabatic index, p the pressure, $\boldsymbol{\kappa} \equiv \frac{1}{2B^4}(\boldsymbol{B} \times \nabla(2\mu_0 p + B^2)) \times \boldsymbol{B}$ the curvature of the magnetic field lines [21, p.736], $\boldsymbol{\xi}^*$ the complex conjugate of $\boldsymbol{\xi}$, $\boldsymbol{n}$ the unit vector perpendicular to the surface, $\boldsymbol{Q_V}$ the vacuum magnetic field perturbation and $\sigma = \frac{\boldsymbol{J} \cdot \boldsymbol{B}}{B^2}$ proportional to the parallel current. Because of the way it is written here, it can easily be seen that the first two (positive) terms from equation (2.16) stabilize the plasma, whereas the last two can be destabilizing. Separately, those two can be recognized to be pressure gradient dependent or parallel current density dependent.

2.2.2 MHD instabilities: a description of different modes

In this graduation project, MHD is used to look at maximum achievable stable pedestal height. The height of the pedestal in H-mode is important because the edge of the plasma adds to the total stored energy of the plasma relatively much, since this is a volume integral of the pressure. As stated in section 1, this pedestal height is not limited by transport, but by the existence of MHD instabilities with ELMs (Edge Localized Modes) as a consequence. In these periodic releases of particles

(and energy), the pressure slightly drops to a point in which the pedestal is stable, herewith releasing particles and energy. It then raises again until the pedestal reaches a point of instability, completing a cycle of the periodicity. ELMs can be a serious problem for ITER if they are not controlled due to doing damage to the wall. Because of the size of ITER, energy released in ELMs is larger than in current devices and thus the first wall components get damage faster. There are two ideal MHD modes that are known to become unstable during an ELM and are therefore the main candidate for a theory to explain the ELMs [22]. These are the peeling modes and the ballooning modes.

The configuration of the magnetic field is important for these instabilities. One way to express this configuration is through so-called toroidal (n) and poloidal (m) mode numbers. These indicate the periodicity in toroidal (n) and poloidal (m) direction. An important quantity connected to this is the safety factor q, mathematically expressed as $q = \frac{rB_t}{RB_p}$. If this safety factor is equal to a rational number, $q = l/k$, field lines close on themselves after l poloidal and k toroidal rotations. A special case exists when $q \approx m/n$. At the radial point where this is the case, the individual Fourier harmonics locally resonate with the modes, so that instabilities are centered around these rational flux surfaces. The shear, defined as the radial derivative of the safety factor $s = \frac{\psi}{q}\frac{dq}{d\psi}$, increases the field line bending [23], which is known to be stabilizing, and it can be seen from e.g. [20, equation (3.9)], that shear increases this effect.

Peeling and ballooning instabilities can be distinguished by looking at the radial structure of their Fourier harmonics, in which one harmonic corresponds to a single poloidal mode number. The superposition of all Fourier harmonics, give a mode structure for one toroidal mode number, which can be looked at separately because toroidal harmonics are decoupled in axisymmetric equilibria. The complete structure has an accompanying growth rate for the instability, equal to the square root of the imaginary part of the eigenvalue. Mode structures for a typical peeling mode (2.3b) and ballooning mode (2.3a) are shown in 3D in figure 2.3.

Ballooning modes exist because of pressure gradients. Mathematically, the destabilizing term is represented by the third term in equation (2.16), $-2(\boldsymbol{\xi} \cdot \nabla p)(\boldsymbol{\kappa} \cdot \boldsymbol{\xi}^*)$, and these are only destabilizing at the low-field side of the plasma. This is because the curvature generally points toward the center of the tokamak, whereas the pressure gradient always points towards the magnetic axis of the plasma. Therefore at the high field side they are opposite (negative sign from the dot product gives a positive term in equation (2.16) which means stability according to the energy principle, as explained in section 2.2.1), while they are parallel at the low field side (negative term means instability). Ballooning modes will thus only be destabilizing at the low field side of the plasma, while being stabilizing at the high field side, as can be seen in figure 2.3a. Here the low field side is the outboard side of the tokamak, whereas the high field side is towards the center of the tokamak. Also, the amplitudes of the harmonics exactly at the edge are zero.

On the other hand, there are peeling modes, which are also edge instabilities, but not bound to any particular poloidal location. Mathematically described by the fourth term in equation (2.16), $-\sigma(\boldsymbol{\xi}^* \times \boldsymbol{B}) \cdot \overline{\boldsymbol{Q}}$, these modes are driven by a finite current density at the edge of the plasma. In mode structures, a finite amplitude of some harmonics is seen at the edge of the plasma and it is often seen that there is one harmonic having a higher amplitude compared to the others. The definition

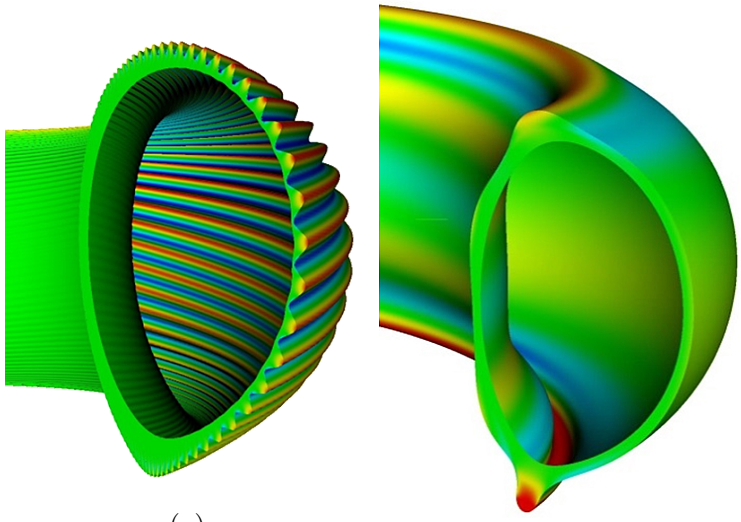

(a) (b)

Figure 2.3: A typical mode structure for a ballooning mode (a), in this case $n = 32$ and a kink-peeling mode (b), for $n = 1$, are shown in 3D. The color or deformation of the surface give a measure for the amplitude of the perturbation. Both can be seen to be localized at the edge of the plasma, with the ballooning mode only being at the low-field side and the peeling mode not dependent on poloidal angle. Figures are taken from [24, Figure 2]

.

of the peeling mode is not clearly defined, though this is a common definition. The perturbation of the plasma edge leads to magnetic structures containing O-points or X-points, which can only be calculated by either taking resistivity into account or adding a surrounding perturbable vacuum, since field lines can't reconnect in ideal MHD and flux surfaces have to be conserved. Since ITER will have a large bootstrap current compared to current devices,

this edge parallel current may decrease stability as compared to current devices and it is expected to have a negative influence on the occurrence of ELMs in ITER.

Peeling and ballooning modes separately are both mathematical extremes, but it is known that in practice, in general, a combination of those modes exists. These coupled modes are called peeling-ballooning modes. For ELMS, high toroidal mode numbers (high-n modes) have been found to be important in general. In some experiments, though, $n = 3$ modes leading to ELMs have also been seen. Altogether, these modes limit the height of the edge pedestal, thus limiting confinement and fusion gain.[25]

Two other modes will also be of importance in this work. These are named (external) kink modes and infernal modes. External kink modes are very similar to peeling modes (which are also external), although instead of being caused by finite values of current density at the edge, it is defined by current density gradients. Being external here refers to the finite value at the edge of the plasma, whereas internal modes have an amplitude of zero at the edge. Because they are caused just by current density gradients, kink modes can also occur in the core of the plasma, then appropriately called internal kink modes, whereas peeling modes are always external. In practice external kink and peeling modes are both present, so that

they are be referred to as kink-peeling modes. Infernal modes are very different from these current density driven modes. They are always internal modes, caused by pressure gradients in a region of low shear. [26] These modes can limit plasma operational space in the center of the plasma, which can lead to disruptions.

2.2.3 HELENA

Equilibria are states in which the plasma is confined and the plasma parameters don't change in time, mathematically expressed by $\partial/\partial t = 0$. For a static equilibrium, there are also no flows involved: $\boldsymbol{v} = 0$. Plugging this into the ideal MHD equations (2.1)-(2.7), this leaves us with the following three equations for static equilibria, which represent the balance of pressure gradient and magnetic force [14]:

$$\boldsymbol{J} \times \boldsymbol{B} = \nabla p, \tag{2.19}$$

$$\nabla \times \boldsymbol{B} = \mu_0 \boldsymbol{J}, \tag{2.20}$$

$$\nabla \cdot \boldsymbol{B} = 0. \tag{2.21}$$

Since a tokamak is a toroidally symmetric device, the axisymmetry can be used to describe the plasma in 2D, although in practice this isn't perfectly valid because the real plasma deviates slightly from axisymmetry due to multiple effects. In such an axisymmetric case, the equilibrium can be described by the Grad-Shafranov equation. A full derivation can be found for example in [14, paragraph 6.2], but is outside the scope of this report. $\boldsymbol{B}$ and $\boldsymbol{J}$ can be derived from equations (2.20) and (2.21) as

$$\boldsymbol{B} = \frac{1}{R}\nabla\psi \times \boldsymbol{e_\phi} + \frac{F}{R}\boldsymbol{e_\phi} \tag{2.22}$$

and

$$\mu_0 \boldsymbol{J} = \frac{1}{R}\frac{dF}{d\psi}\nabla\psi \times \boldsymbol{e_\phi} - \frac{1}{R}\Delta^*\psi \boldsymbol{e_\phi}, \tag{2.23}$$

with ψ is the poloidal magnetic flux (which can be seen as a radial coordinate because of the flux surfaces), $\boldsymbol{e_\phi}$ the unit vector in the toroidal direction, R the radial coordinate as seen from the center of the tokamak and $F(\psi) \equiv RB_\phi$ a measure for the toroidal magnetic field.

Plugging these into equation (2.19), results in the Grad-Shafranov equation:

$$\Delta^*\psi = -\mu_0 R^2 \frac{dp}{d\psi} - F\frac{dF}{d\psi}. \tag{2.24}$$

with $p(\psi)$ the pressure and the operator Δ^* defined as $\Delta^*\psi \equiv R^2\nabla \cdot \left(\frac{\nabla\psi}{R^2}\right)$.
In HELENA, bicubic Hermite elements are used to numerically solve the Grad-Shafranov equation, calculating values of flux surface quantities. It also calculated the straight field line coordinate system from which MISHKA can calculate stability. [27]

2.2.4 MISHKA

From perturbing the equilibria calculated by HELENA, (in)stability can be determined. Starting with the ideal MHD equations for static equilibria (2.19)-(2.21),

the quantities $\rho, \boldsymbol{v}, \boldsymbol{B}$ and p are linearized as $Q = Q_0 + Q_1$ with Q_0 the equilibrium quantity and Q_1 the perturbed quantity, separating the spatial and time-dependent parts according to $Q(\boldsymbol{r}, t) = \widetilde{Q}(\boldsymbol{r})e^{\lambda t}$, so that $\lambda = -i\omega$, with ω the perturbation frequency. The equilibrium velocity is equal to zero, since only static equilibria are considered: $\boldsymbol{v_0} = 0$. The perturbed magnetic field is then written as the curl of a perturbed vector potential: $\boldsymbol{B_1} = \nabla \times \boldsymbol{A}$. The perturbed vector potential is then discretized through:

$$A(\boldsymbol{r}, t) = e^{\lambda t} \sum_m A_{mn}(\psi) e^{in\phi + im\theta} \tag{2.25}$$

with λ, n a toroidal mode number and the summation over a finite number of poloidal mode numbers m. The Galerkin method is then used to solve as an eigenvalue problem for λ, giving stability for $\lambda < 0$ (mode amplitude decaying in time) and instability for $\lambda > 0$ (mode amplitude increasing in time). In contrary to the axisymmetric equilibrium, the stability calculations are done in three dimensions. [28]

2.3 Core pressure effects on MHD pedestal stability

The pressure at the top of the pedestal (the height of the pedestal), is, as aforementioned, an important ingredient in the recipe of fusion power on earth, because of the relatively large increase in stored plasma energy with the pedestal height. It is seen in experiments that this height depends on the pressure in the core (although this is often not taken into account in transport codes) [30]. It is also seen that the pedestal height depends on the Shafranov shift, which is a displacement of the flux surfaces in the radial direction towards the low field side [31]. It is schematically shown in figure 2.4 and can mathematically be approximated by $\frac{\Delta(0)}{a} \approx \epsilon\beta_p \frac{0.342}{1+5.7(p_{ped}/p_0)^{1/3}}$, as was found by Javier Artola in unpublished work at ITER, with $\Delta(0)$ the Shafranov shift at the magnetic axis, a the minor radius of the plasma, $\epsilon = \frac{a}{R}$, the aspect ratio, which is the ratio of minor to major radius, β_p is the poloidal beta, p_{ped} the pressure at the top of the pedestal and p_0 the pressure in the core (at $\psi = 0$). The Shafranov shift is larger for higher core pressures as a result of the MHD equations, as seen from the mentioned equation.

A model for this effect can be obtained, when defining the pedestal pressure, p_{ped}, as the pressure at the top of the pedestal. Using this, the poloidal beta, β_p or $\beta_{p,tot}$, defined as the ratio of the kinetic energy of the plasma (volume integral over the pressure profile) and poloidal magnetic field energy, $\beta_{p,tot} = \frac{<p>}{B_p^2/2\mu_0}$, can be separated in two parts. The pedestal poloidal beta, $\beta_{p,ped} = \frac{<p>_{ped}}{B_p^2/2\mu_0}$, in which only the integral of the pressure up to p_{ped} is taken into account, which is mathematically given by

$$\frac{< p >_{ped}}{4\pi^2 aR} = \int_0^{\psi_{N,ped}} p_{ped} d\psi_N + \int_{\psi_{N,ped}}^1 p(\psi_N) d\psi_N \tag{2.26}$$

with ψ_{ped} the ψ-coordinate at which the pedestal height is maximum. Also, the core poloidal beta is defined, $\beta_{p,core} = \frac{<p>_{core}}{B_p^2/2\mu_0}$, in which the integral is taken from p_{ped} upto the maximum value as

$$\frac{< p >_{core}}{4\pi^2 aR} = \int_0^{\psi_{N,ped}} \left(p(\psi) - p_{ped}\right) d\psi_N. \tag{2.27}$$

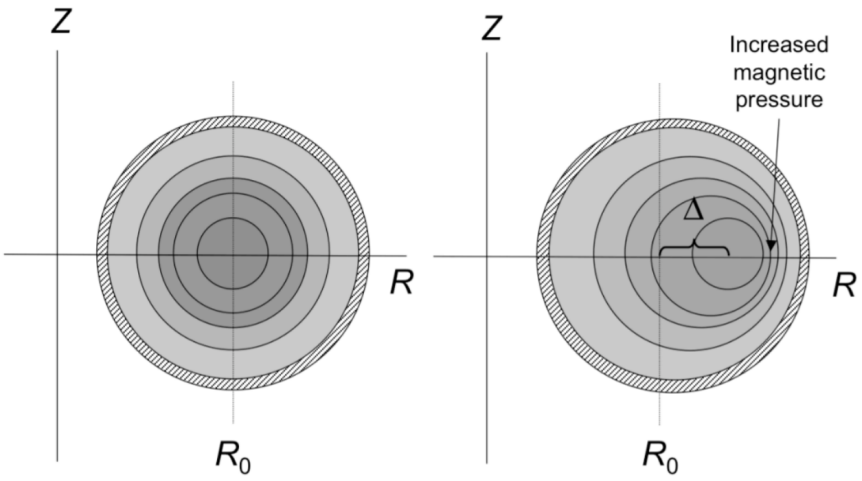

Figure 2.4: Schematic view of the Shafranov Shift effect. Due to plasma pressure, the magnetic axis shifts from the center of the plasma (left) to further to the outboard side (right). The difference in radial coordinate is the Shafranov shift, given by Δ, or $\Delta(0)$, when spoken about the shift at the magnetic axis, although it can be given at any coordinate. [29]

This way, both add up to the total poloidal beta: $\beta_{p,tot} = \beta_{p,ped} + \beta_{p,core}$. This is also shown schematically in figure 1.1.

The interplay between the core and the pressure has been researched before (see e.g. [1]) and it is believed this is a self-amplifying feedback mechanism, in which an increase in the core leads to a larger stable pedestal height through a higher Shafranov shift, which then again raises the pressure in the core because of the profile stiffness of temperature and pressure profiles, i.e. it is being forced to keep the same profile shape as a result of the critical gradient everywhere in the profile. However, in this research, it was also found that this effect might be limited for high normalized β, $\beta_N = \beta_{tor}\frac{aB_T}{I_P}$ (in which $\beta_{tor} = \frac{<p>}{B_t^2/2\mu_0}$), which raises questions on its applicability to ITER.

In practical situations the benefits of this effect are taken advantage of by increasing the core pressure through heating, which kicks off he feedback mechanism. In this model the two parts of the feedback mechanism are treated separately. Firstly, the maximal attainable pedestal height is a function of the total pressure through MHD, driven by the Shafranov shift. HELENA- and MISHKA-simulations are used to obtain a relation for this part of the model. The relation is assumed to be a power law:

$$\beta_{p,ped} \propto \beta_{p,tot}^{\alpha} \tag{2.28}$$

in which α is the parameter that is obtained from the results of the simulations.

The second part of the model, the stiffness, gives the coupling to heating input power. This is defined as a relation for the ratio of the core and the pedestal, in which again a power law is assumed:

$$\frac{\beta_{p,core}}{\beta_{p,ped}} \propto P_{in}^{\delta} \tag{2.29}$$

with P_{in} the input power and δ representing the stiffness.

Ultimately, this can then be compared to a scaling law, in which results from different fusion reactors are used to obtain a relation between the energy confinement time and several important quantities for fusion, of which one is the input power. The scaling law that is used for ITER H-mode, IPB98(y,2) [3, p.2204], gives a relation between the thermal energy confinement time in ELMy H-mode (in seconds) and important engineering variables:

$$\tau_{E,th}^{ELMy} = 0.0562 I^{0.093} B^{0.15} P^{-0.69} n^{0.41} M^{0.19} R^{1.97} \epsilon^{0.58} \kappa_a^{0.78}, \tag{2.30}$$

with I the plasma current in MA, B the toroidal magnetic field in T, P the loss power in MW, n the line average density in $10^{19}\mathrm{m}^{-3}$, M the average ion mass in AMU, R the major radius in m, ϵ the inverse aspect ratio, the ratio between minor and major ratio and κ_a an alternate definition (see [3, section 6.4]) of the elongation, the ratio between the long and short side in an elliptically shaped plasma. The total stored energy can then be written as $W_{tot} = \tau_E \cdot P$, which is equal to the volume integrated pressure so that it is equal to $\beta_{p,tot}$ multiplied by a constant factor. From this, a relation between energy and the input power is obtained, according to:

$$W_{tot} \propto P_{in}^{\gamma} \tag{2.31}$$

with $\gamma = 0.31$ in IPB98(y,2). This scaling law does not mention different behavior for pedestal and core. Implicitly, it is assumed that they scale linearly, which would be given by $\alpha = 1$ in equation (2.28). However, since a limit to the effect, or at least a faster growing $\beta_{p,core}$ than $\beta_{p,ped}$, is expected, a more realistic value of α would be positive but smaller than 1.

2.4 ITER confinement and scaling law comparison

Combining equations (2.28) and (2.29), can then give us a comparison of this model in which core and edge are treated separately, to compare with both experimental data in which this is looked at separately (i.e. [2]) and the aforementioned scaling law in which there is no distinction. This is done by rewriting

$$\beta_{p,core} = \beta_{p,tot} - \beta_{p,ped} \tag{2.32}$$

and replacing $\beta_{p,ped}$ by using equation (2.28). Inserting this in equation (2.29), results in

$$\frac{\beta_{p,tot} - \beta_{p,ped}}{\beta_{p,ped}} = \frac{\beta_{p,tot}}{\beta_{p,tot}^{\alpha}} - 1 = C_{\beta W} \cdot W_{tot}^{1-\alpha} - 1 \tag{2.33}$$

with $C_{\beta W}$ the constant to convert β into energy. Because of this relation only being a multiplication with this constant, in this context they can be treated similarly within the same formulas. Alltogether, this then leads to

$$W_{tot} = \left(C_1 \left(1 + C_2 P_{in}^{\delta}\right)\right)^{\frac{1}{1-\alpha}} \tag{2.34}$$

with C_1 the proportionality constant of equation (2.28) and C_2 of equation (2.29), both here including a factor to write as energy instead of β). Since this can not directly be compared to equation (2.31), the input power is calculated from some values of W_{tot} obtained from the MHD simulations. The obtained values of W_{tot}

can then be plotted against the values of input power P_{in}. Since this is not exactly according to the power law relation of equation (2.31), another fit has to be done. These calculated values of W_{tot} are fitted against that same power law relation, $W_{tot} \propto P_{in}^{\gamma_{fit}}$, so that γ_{fit} is obtained from the fit. This can then be compared to the actual γ from the IPB98((y,2) scaling law [3].

Another thing that has to be taken into account is that γ also has an upper limit, which is due to plasma control reasons. In order to keep manual control over the plasma, it is necessary that a temperature perturbation decays in time. Otherwise a temperature change results in a temperature excursion in which the perturbation amplifies itself. In this unstable burn the plasma fusion power controls itself. It is found from internal calculations at ITER that this is limited by $\gamma \leq 0.5$, in which case the state of the plasma can be controlled more actively, which is desired.

Chapter 3

Numerical method

As discussed in section 2.3, heating the core of the plasma affects the edge stability. The way how the core pressure and edge stability influence each other, then gives information on how the edge pedestal can be increased in ITER. Because of this, the stored plasma energy is increased and thus the energy confinement time, so that confinement is improved. The theory was discussed in section 2.3 and in this chapter the methods are described in more detail. Two numerical codes are used: HELENA (described in section 2.2.3) is used to calculate an axisymmetric equilibrium for the different pressure profiles and MISHKA (described in section 2.2.4) is used to calculate their stability.

3.1 HELENA parameters

A HELENA input file is generated by ASTRA simulations (ASTRA is a transport code) that are done for different ITER scenarios by Alexei Polevoi. These have to be adapted because of the different pressure profiles and an example of one of the adapted HELENA input files is given in Appendix C.1. Also, an example of an input file used for MISHKA is given in Appendix C.2.

In order to create different pressure profiles, two parameters are added into HELENA (`betap_ped` and `corep` in the input file) to change the core pressure and the pedestal height separately. Preliminary work for this was done by Javier Artola in unpublished work during his Master's project. It is shown in figure 3.1 how these parameters change the pressure profile. The `pedestal beta` parameter changes the height of the pedestal so that the integrated pressure up to the pedestal height gives an equal $\beta_{p,ped}$, as discussed in section 2.3 through equation (2.26) to that of the input file. The core pressure is then changed by multiplying the whole $\frac{dp}{d\psi}$ profile with the function

$$-0.5 \cdot (\tanh\left(\frac{\sqrt{\psi} - \texttt{psiped}}{0.02}\right) - 1) \cdot (\texttt{corep} - 1) + 1. \tag{3.1}$$

This way the core is multiplied by a factor `corep` smoothly changing to a multiplication of just one at the edge, through a hyperbolic tangent. As a consequence, only the core pressure changes whereas the edge pedestal stays the same. Note that $\beta_{p,ped}$ is determined in an iterative process by a multiplication of the entire normalized profile so that it converges to a pressure profile in which $\beta_{p,ped}$ is equal to the set value. This means that the core pressure and core profile change along with

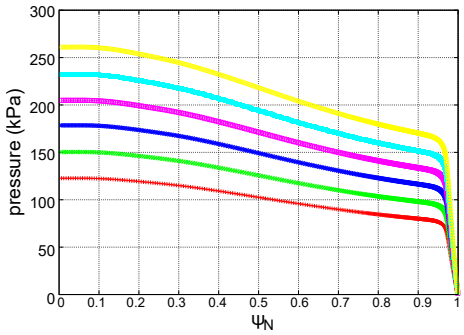

(a) $\beta_{p,ped}$ changed, while core pressure parameter is kept constant.

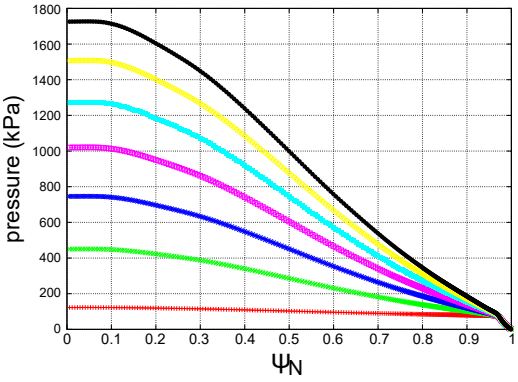

(b) Core pressure parameter changed, while $\beta_{p,ped}$ is kept constant.

Figure 3.1: Shown how the pressure profile is changed with the two pressure profile parameters that are implemented in HELENA. Both are changed separately, in (a) $\beta_{p,ped}$ and in (b) the core pressure parameter.

the change in $\beta_{p,ped}$ and thus $\beta_{p,core}$ is not completely independent of `betap_ped`. However, since a parameter scan is done in a 2D parameter space, this is not a problem. The `corep` parameter can be changed as a function of $\beta_{p,ped}$ so that all of the parameter space, where an equilibrium exists, can be covered.

In order to use these parameters, some changes in the HELENA input file have to be made compared to the ASTRA output. Firstly the point of the start of the pedestal has to be determined. For this project, this is done using the second derivative of the pressure profile to determine the top of the pedestal. For the reference case, the value of the second derivative at the pedestal top radius is taken and when the pedestal is made wider, this same value of the second derivative is found, so that the new value of ψ at which the pedestal top is, is an actual grid point in the coordinate system. The `psiped` input parameter, being the psi coordinate at which the pedestal top is located, is then used in the calculation of $\beta_{p,ped}$.

Also, by changing this `psiped` parameter as a function of $\beta_{p,ped}$, the pedestal width can be varied. In this work the assumed relation between the pedestal width and height is $\Delta_{\psi_N} \propto \beta_{p,ped}^{1/2}$, according to the EPED pedestal model [32], which results in an approximately constant pedestal width in real space coordinates (in meters). Simulations for each scenario are done for both a constant and a varying pedestal width. The different scenarios are discussed in section 3.3.

A final point is to realistically increase bootstrap current with pedestal height. In the HELENA file the bootstrap current is calculated, after the simulations are done, by a formula as derived in [33]. The height of the peak of the bootstrap current is then manually determined for some cases to approximately being the same as is calculated. Also the current at the edge is forced to approximately zero. This can be seen in figure 3.2: the blue line adapted to the same height as the red line, which is the calculated bootstrap current. A formula for the bootstrap current density peak height as function of $\beta_{p,ped}$ is then determined by an interpolation of the test cases. For this comprehensive model this is thought to be sufficient, since differences in height are rather small, as are the deviations from zero at the edge. These are found to be the most important influences on edge stability, so that this should make the model accurate enough. In this process, the total current is kept constant.

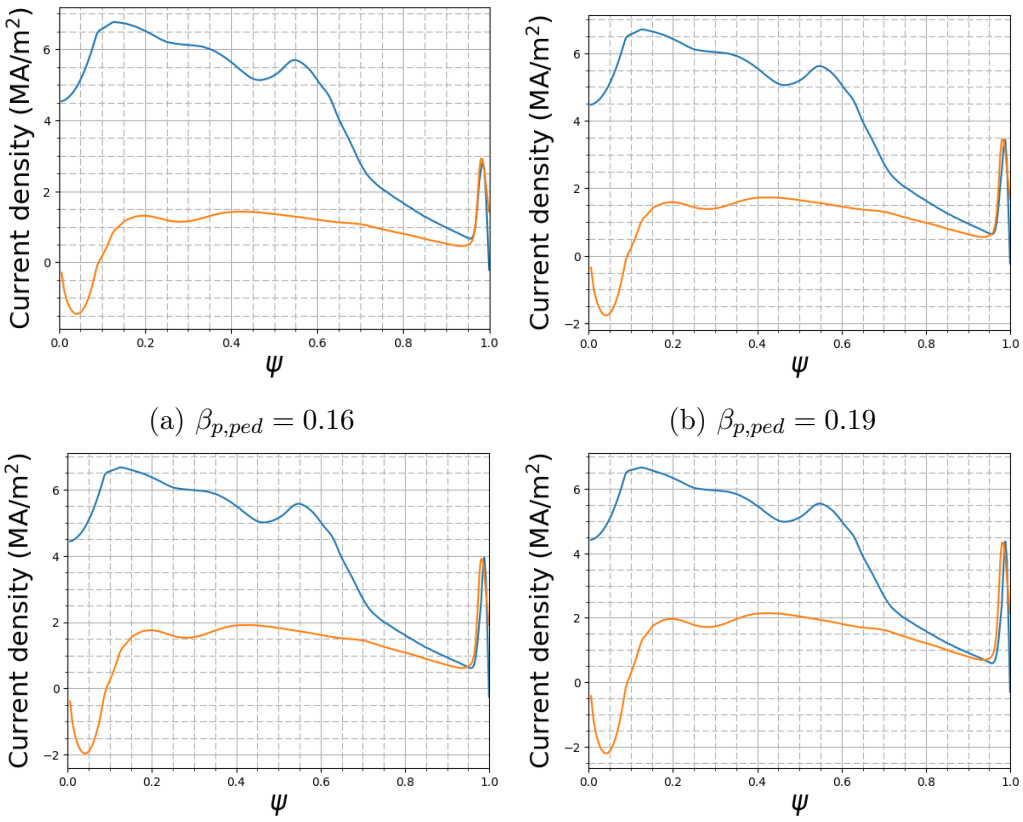

(a) $\beta_{p,ped} = 0.16$

(b) $\beta_{p,ped} = 0.19$

(c) $\beta_{p,ped} = 0.215$

(d) $\beta_{p,ped} = 0.24$

Figure 3.2: Change of the bootstrap current for different $\beta'_{p,ped}s$, for the 10MA scenario with constant pedestal width. In blue the used current profile, with the bootstrap current manually matched at the edge, and in orange the bootstrap current as calculated by HELENA with the neoclassical formula after calculation of the equilibrium. Since it is assumed that bootstrap current is dominant only at the edge, but not in the core, it only matches there.

3.2 MISHKA parameters

With the calculated equilibrium, MISHKA then calculates the stability for a range of mode numbers and grid accumulation is used near the edge (for both HELENA and MISHKA) in order to get better results. The range of mode numbers is typically $n = [2-40]$, which was chosen after examination of the modes that typically occur in each case. An important parameter is `sbegin`. This sets a lower limit to the radial coordinate for which stability is calculated, so that only $s = \sqrt{\psi_N} \geq$ `sbegin` is taken into account. This is used to focus on the edge, without taking all internal modes into account. Also, the $n = 1$ modes are left out of consideration because these are known to possibly cause internal kink modes, in the core of the plasma, before the pedestal limit is reached. Since for this work, pedestal stability is the main interest, these instabilities in the core of the plasma are not looked at and therefore $n = 1$ is omitted. In this research `sbegin` is taken to be 0.5. Also, convergence is checked by comparing the eigenvalues calculated in the last two iterations. If this relative change is smaller than 10^{-6} it is said to be converged. If a solution is converged the absolute value of the eigenvalue is also check and if this is smaller than 10^{-4} it is assumed to be stable. Also, since both HELENA and MISHKA, can't numerically deal with the X-point in the ITER-plasma, only coordinates $\psi \leq 0.99$ are taken into account.

The coupling of this code is done through a python script that submits jobs to the ITER cluster. That way around one hundred jobs are done at the same time, each doing one HELENA run and subsequent MISHKA run, with a lot of different MISHKA runs (different toroidal mode numbers) for every equilibrium. Each job uses HELENA and MISHKA files with parameters changed to calculate equilibrium for a certain pressure profile (change several HELENA parameters) and do this for every toroidal mode number (changed in MISHKA input file). Simulations take about one to four days per scenario. This is only for constant or varying pedestal width, so both takes double that time.

3.3 A look at different ITER scenarios

In order to prepare as well as possible to obtain the ITER goals, experiments are planned in detail. These are all described in internal documentation on which the contents of this section are based. Globally, there are four phases. A first plasma phase, in which it is shown that a (hydrogen) plasma can be created, although it doesn't have the properties of a fusion plasma yet. Only at the end of this phase, the first wall components are installed. After that, the Hydrogen/Helium phase is started, in which fusion plasmas are researched, so it can be seen if results from current machines and models are applicable to ITER. At the end of this phase, all heating systems should be available. Then the Deuterium (D) phase is started, in which more studies are done, e.g. on H-mode and (tungsten) impurities and nuclear operation is started. Also, in this phase the full machine commissioning is completed (completing heating and current drive systems, diagnostics and more). The last phase is the Deuterium-Tritium (DT) phase, in which it is planned to achieve a fusion gain (the ratio between fusion power produced in the plasma and the input power) of $Q = 10$, according to the mission of $Q \geq 10$. After this is accomplished, non-inductively driven plasmas are also planned and finally the full

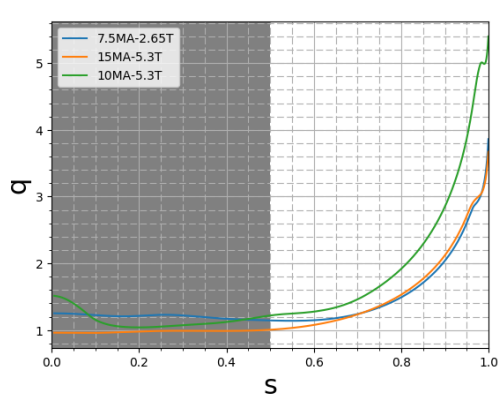

(a) Safety factor profiles

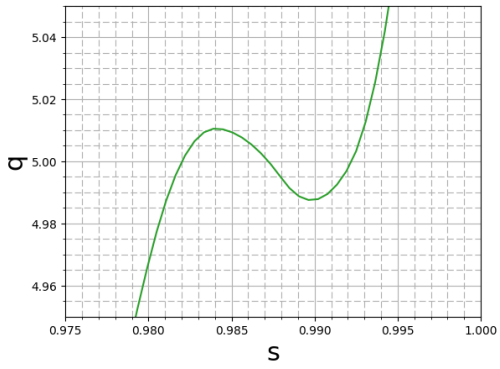

(b) Zoom on reversed global shear in the q profile of the 10MA scenario.

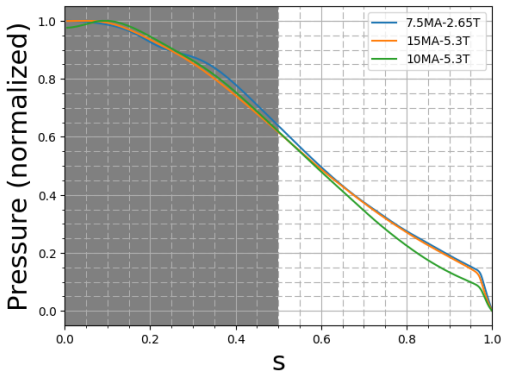

(c) Pressure profiles

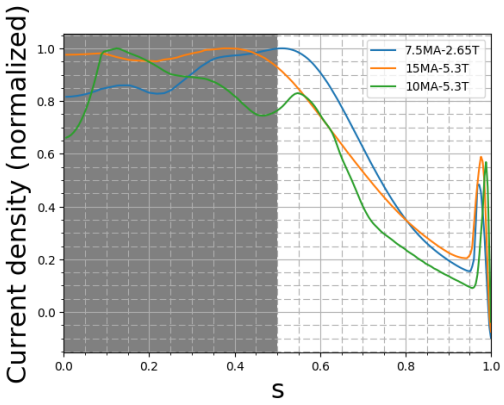

(d) Current density profiles

Figure 3.4: Safety factor (a), pressure (c) and current density (d) profiles for all three different scenarios in which $s <= 0.5$ (the grey area) is not taken into account. In (b), a small part of the 10MA q-profile is shown, in which there is a negative global shear, that is likely to be the cause of the region of low-n kink-peeling modes. Real values can be found in figure A.4 in appendix A.2, with pressure center values of around 1 MPa (15MA), 200 kPa (7.5 MA) and 900 kPa (10MA), and current density center values around 8 MA/m^2 (15MA), 2 MA/m^2 (7.5MA) and 900 MA/m^2.(10MA)

potential of ITER fusion power amongst other research plans, although these are not planned in full detail yet.

For this work, three scenarios are looked at in detail. A 15MA/5.3T full current, full field scenario, a 7.5MA/2.65T half current, half field scenario, which are both inductive scenarios and a 10MA/5.3T steady-state scenario. The geometry is shown in figure 3.3 for the 15MA case, although differences in geometries in the different scenarios are negligible. Other details of all of them are discussed in more detail below.

For the three cases, the normalized profiles of the safety factor, pressure and current density of the reference case are plotted in figure 3.4, with the grey areas not being taken into account in the stability calculations. It stands out that the safety factor at the edge is much higher for the 10MA case, which is due to the lower current with the same magnetic field ($q = \frac{rB_t}{RB_p} \propto \frac{B_t}{I_t}$). Also, the pedestal β of the 10MA case is relatively much lower, although absolutely that is not the case (150 kPa (15MA), 100 kPa (10MA), 30 kPa (7.5MA)), as can be seen from figure A.4 in

Appendix A.2.

3.3.1 Q=10 scenario: 15MA-5.3T

Firstly, a 15MA/5.3T (full current, full magnetic field) scenario, as part of the DT phase is chosen. In this scenario the power gain should reach $Q = 10$. This is chosen, because of the importance of this scenario in the planning of ITER: it will be showing that the ITER goal of $Q \geq 10$ can be accomplished. In order to do this, the core-edge feedback mechanism can be especially important. To reach H-mode 50MW of auxiliary power is used. In this scenario an average electron density of $< n_e >= 11.2 \cdot 10^{19}$, edge safety factor of $q_{95} = 3.2$, core temperatures of $T_{e0} \approx T_{i0} \approx 24keV$ and energy confinement time of $\tau_E = 3.7s$ are expected to be achieved.

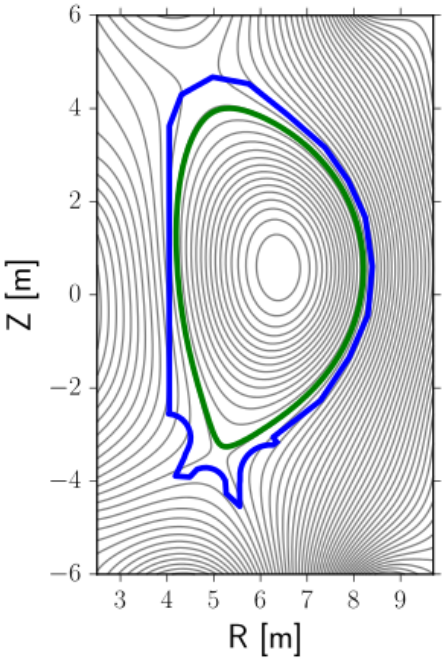

Figure 3.3: Geometry of an ITER plasma, with the boundary of the plasma shown in green and the vacuum vessel in blue. This is for the 15MA scenario, but all plasma shapes are similar.

3.3.2 Half field-Half current scenario: 7.5MA-2.65T

The 7.5MA/2.65T used is from the Deuterium phase, in the ITER planning it is done to investigate properties of H-mode in ITER and to look at how scaling laws extrapolate to ITER. The amount of auxiliary power used here 53MW. Experiments can then be done in preparation of increasing both current and field. This scenario is chosen because normalized MHD quantities are the same as the 15MA/5.3T scenario, so it can be compared to this scenario. The difference is in the profiles that are different. Especially note the bump in the current density profile, the (smaller) bump in the pressure profile in figure 3.4 and the safety factor being constant further towards the edge (up to around $s \geq 0.6$. This is caused by off-axis neutral beam injection, which is also slightly larger ($P_{NBI} \approx 12MW$) than for the Q=10 scenario ($P_{NBI} \approx 10MW$). The deviation from the axis is because at lower density, $< n_e >= 3.6 \cdot 10^{19}$ for this scenario, beams penetrate beyond the core. Since the total NBI power is the same, the beam driven current is the same, which means that for the 7.5MA scenario (thus half current) the beam driven fraction is twice as high as for the 15MA scenario. Other parameters are the edge safety factor $q_{95} = 4.0$, electron/ion core temperatures of $T_{e0} = 16keV$ and $T_{i0} = 11keV$ and energy confinement time of $\tau_E = 1.8s$.

3.3.3 Q=5 steady-state scenario: 10MA-2.65T

Finally, a completely different case is chosen with a 10MA/5.3T steady-state scenario, which takes place during the DT phase. It is meant to succeed the ITER goal

of $Q \geq 5$ in steady-state. This scenario is mainly chosen because of the high value of the safety factor at the edge, that is known to be important for edge stability. In this case that is $q_{95} = 5.9$ and in such a scenario these are high because improved confinement and stability are shown in such experiment at current device only for high edge safety factor.

Steady-state refers to the fact that there is no inductively driven current, i.e. no ohmic heating after start-up, as opposed to the inductive scenarios, where most current is driven inductively, or the hybrid scenarios, in which about half of the current is driven inductively and the other half non-inductively. Since inductive current drive limits the pulse length, for the steady-state ITER scenarios a longer pulse length is expected. To achieve this non-inductive current, 79.5W of auxiliary power is used. In this scenario, the average density is $< n_e >= 5.9 \cdot 10^{19}$, electron/ion core temperatures of $T_{e0} = 16keV$ and $T_{i0} = 11keV$ and energy confinement time of $\tau_E = 2.6s$.

Chapter 4

Results and discussion

Simulations can be done as described in chapter 3, covering a range in the parameter space of $\beta_{p,ped}$ and β_N, with a certain range of toroidal mode numbers. The $n = 1$ modes are as said not taken into account.

For each scenario discussed in section 3.3, stability is determined for all toroidal mode numbers for all different pressure profiles. This is done for both constant and varying pedestal width. The most unstable point is plotted in the stability graphs (figures 4.1, 4.3, 4.5 and 4.7), in which stable points are empty circles and otherwise the most unstable toroidal mode number is given by the color. There are also some empty spots, which are points where an instability was calculated by MISHKA but after examining the mode structure, these are considered to be only of numerical nature and not real instabilities. For the core modes that are found around $s = 0.5$, the plots of the mode structures are shown with a range in radial coordinates of $s \geq 0.1$ and without using grid accumulation near the edge. This is done to see the complete mode with more points in the region where it exists. This is done only for a few points (for all scenarios) after the regular simulation were done. In these regular simulations all points are done with grid accumulation at the edge and $s \geq 0.5$ in order to focus on edge modes also when core modes are found. By looking at a couple of these core instabilities, it was concluded that all of them are real instabilities. The dark crosses in the stability graphs represent the reference cases, which are directly taken from ASTRA simulations.

4.1 15MA-5.3T constant pedestal width

For the 15MA case, the stability graph is given in figure 4.1 and the positive relation between maximum achievable pedestal height and β_N clearly shows. It stands out that the reference point ($\beta_{p,ped} \approx 0.135$, $\beta_N \approx 1.95$) is at the boundary of stability limited by the pedestal height. This is not a coincidence, but is enforced by ASTRA. Results of the EPED pedestal stability model [34] are used to push to the limits of edge stability. By using a different approach, namely MISHKA, it is also found in this work that the point is limited by the pedestal height. Besides the limit by pedestal height, there is also a global limit that limits the total pressure. For high β_N, the exact value only slightly depending on $\beta_{p,ped}$, with β_N between 2.7 and 3.1, instabilities are found that lead to a disruption, in which confinement is quickly lost and the plasma is destroyed, herewith doing damage to the machine. Looking at the maximum achievable pedestal heights again, in theory, the path could be

followed from the reference point to higher total and pedestal β, $\beta_N \approx 3.05$ and $\beta_{p,ped} \approx 0.145$, but in practice ITER will not have enough heating power to achieve the complete path. However, if this would be possible and fusion energy is assumed to scale with the core pressure squared, $P_{fus} \propto p_0^2$, an increase in fusion power by a factor of 3.7 (from 0.86 MPa to 1.66 MPa) would theoretically be possible.

To get a better understanding of the instabilities, the mode structure is looked at for a couple of points in the stability graph, as can be seen in figure A.1. The radial dependence of a poloidal harmonic, which are given by $A_{mn}(\phi)$ in equation (2.25), are plotted. These mode structures are made by the so-called 'fast' option in MISHKA, which automatically choses a range of poloidal mode numbers, different for each toroidal mode number, that are resonant, i.e. $m \sim nq$, which causes instabilities. As a consequence, a peaked behavior can be seen in the mode structure, since one line can correspond to different poloidal mode numbers.

What can be seen in this scenario is that instabilities for high β_N are most unstable for a toroidal mode number around $n = 40$, whereas for high $\beta_{p,ped}$ unstable modes are closer to $n = 30$. The unstable modes for high $\beta_{p,ped}$ are peeling-ballooning (edge) modes, whereas the unstable modes for high β_N are internal (core) modes, the so-called infernal modes.

The first equilibrium looked at, is an unstable point just at the stable-unstable-boundary, for low β_N, as shown in the lower left plot of figure A.1. Each line gives the radial dependence of the poloidal harmonic, of which the amplitude is given by A_{mn} in equation (2.25). This is clearly an edge mode, and it is recognized as a peeling-ballooning mode, due to, as explained in section 2.2.2, a large part of the harmonics lying within the plasma, although there are also still poloidal harmonics with a finite value at the edge. Going further along the boundary gives similar (slightly broader) peeling-ballooning modes, as is also shown in the upper right graph. These peeling-ballooning modes are also found going to higher $\beta_{p,ped}$ (not shown). However, when going to large values of β_N the mode structure no longer shows an edge instability. For, in this case, starting from $\beta_N \geq 2.8$ (for low $\beta_{p,ped}$), core instabilities can be found, as can be seen in the lower right plot in figure A.1. These core instabilities are called infernal modes, which were already discussed in section 2.2.2. These infernal modes are known to be caused by a combination of a high pressure gradient and low shear. The physical consequence of these infernal modes, has to do with what Troyon discovered already in the 1980's, which is now known as the Troyon limit. This is caused by global kink and ballooning modes as a consequence of global pressure gradients (the total pressure profile considered). As mentioned, this leads to disruptions. It is known that this gives a limit at $\beta_N \approx 4l_i$ [35], with l_i the internal inductance, which is also seen here since $l_i = 0.73$ for this scenario. Growth rates are 0.047 for the infernal mode, $3.9 \cdot 10^{-4}$ for the low β_N peeling-ballooning mode and $3.9 \cdot 10^{-4}$ for the high β_N peeling-ballooning mode.

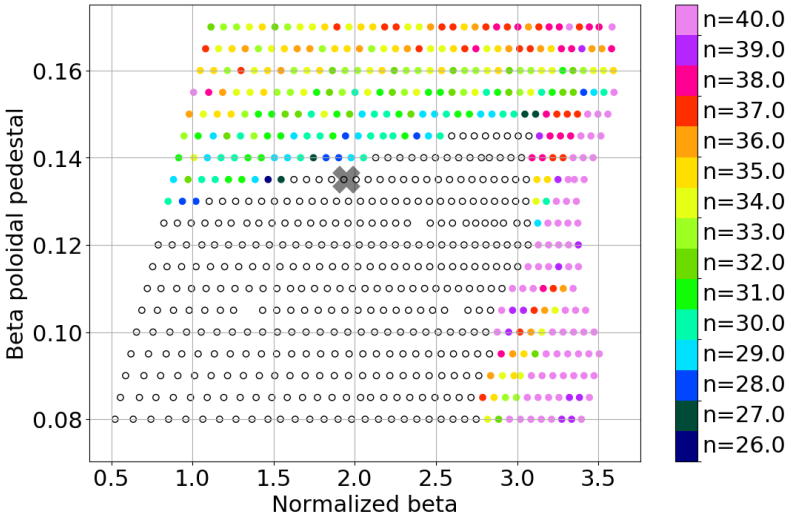

Figure 4.1: Stability graph for the 15MA, 5.3T scenario. $\beta_{p,ped}$ vs β_N, in which for each point the most unstable mode is depicted. Empty circles give stable modes and for the unstable modes, the most unstable toroidal mode number is given by the color. The original ASTRA point is given by the cross.

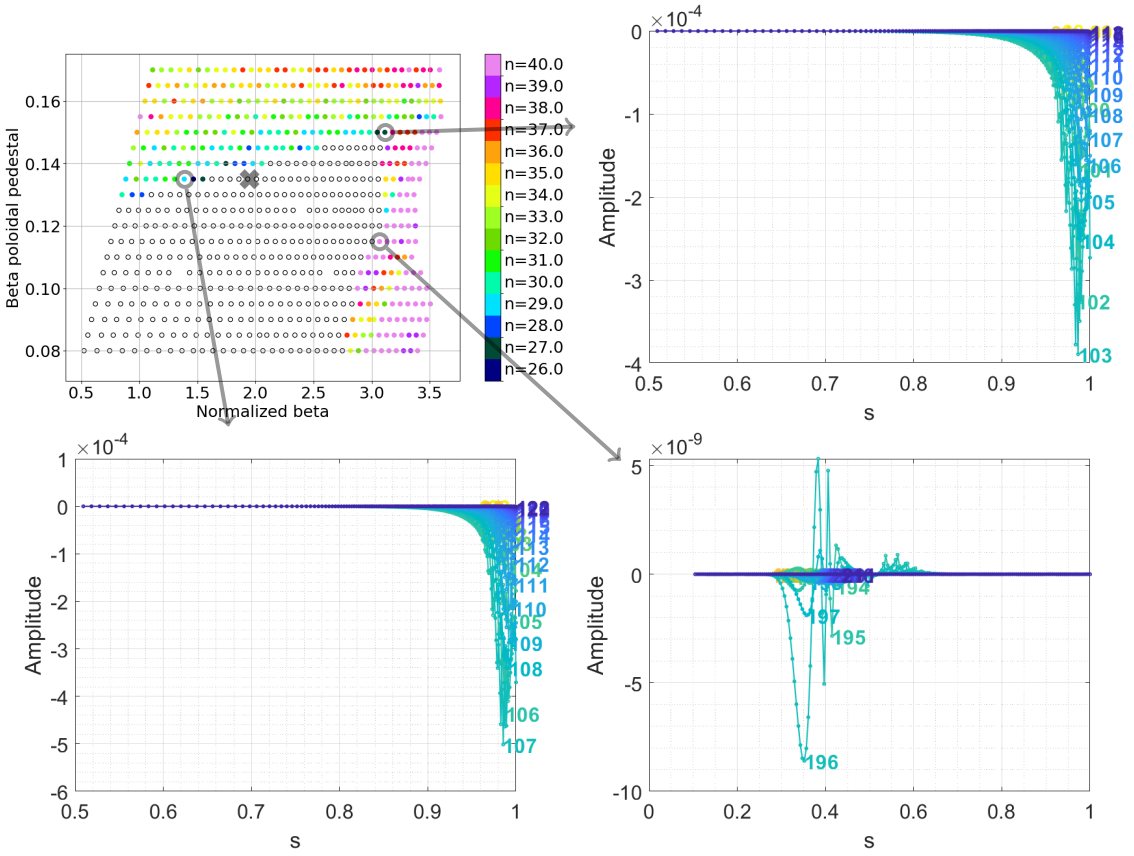

Figure 4.2: Mode structure for three points of the 15MA case with constant pedestal width, with also given which point it is in the stability graph from figure 4.1. For these stability calculations the 'fast' mode of MISHKA is used, in which the mode numbers are chosen automatically.

4.2 7.5MA-2.65T constant pedestal width

The Half current-half field scenario (7.5MA-2.65T) is very similar to the 15MA case. This is also expected, since the combination of half current and half field yields identical normalized MHD quantities. However, due to off-axis neutral beam heating, which is also relatively much more power than for the 15MA case, a combination of a flat q-profile with a steep pressure gradient causes the infernal modes to occur for much smaller β_N, also more depending on $\beta_{p,ped}$, around $\beta_N \approx 1.6 - 2.0$.

The modes that are seen for the 7.5MA scenario, are similar to the 15MA scenario, with peeling-ballooning modes for high $\beta_{p,ped}$ and infernal modes for high β_N, although it can be seen that mode numbers until $n = 60$ are taken into account. This was done because the interval of $n = [2, 40]$ was found to be too narrow, so that higher mode numbers were taking into account to give more details. It can be seen that, indeed, small regions of different mode numbers are found to be the most unstable, with mode number around $n = 50$ for the peeling-ballooning modes. The limit for high β_N is still caused by infernal modes, also with slightly higher toroidal mode numbers going up to $n = 60$ for the most unstable mode. Also, the reference point ($\beta_{p,ped} \approx 0.15$, $\beta_N \approx 2.05$) is not exactly at the most stable pedestal height, but it is very close. This difference can be attributed to effects other than MHD.

Finally, for this scenario, the mode structures, as can be seen in figure 4.4, are almost the same as for the 15MA case. The biggest difference between the 15MA and 7.5MA cases here is the exact structure of the occurring infernal modes, which in the 7.5MA scenario is only consisting of one peak, whereas for the 15MA scenario, it is a broader structure. Growth rates are 0.0037 for the infernal mode, 0.044 for the low β_N peeling-ballooning mode and 0.205 for the high β_N peeling-ballooning mode.

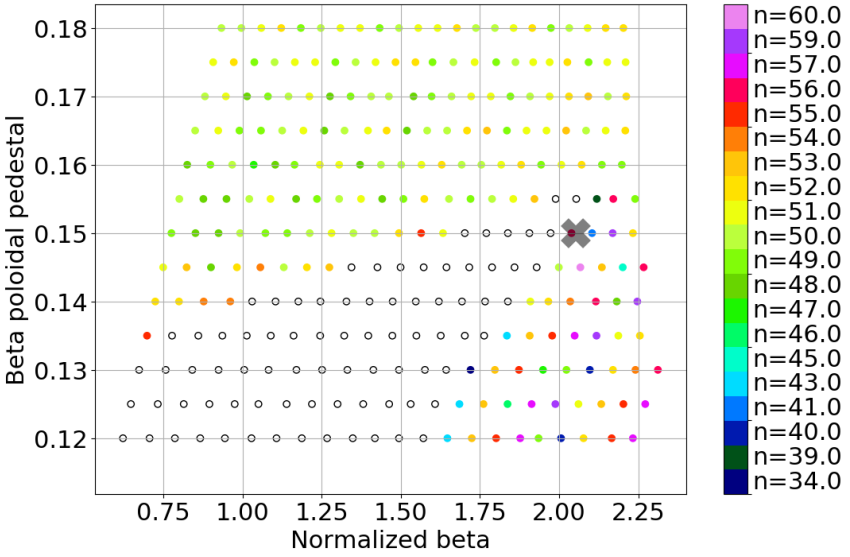

Figure 4.3: Stability graph for the 7.5MA, 2.65T scenario. $\beta_{p,ped}$ vs β_N, in which for each point the most unstable mode is depicted. Empty circles give stable modes and for the unstable modes, the most unstable toroidal mode number is given by the color. The original ASTRA point is given by the cross.

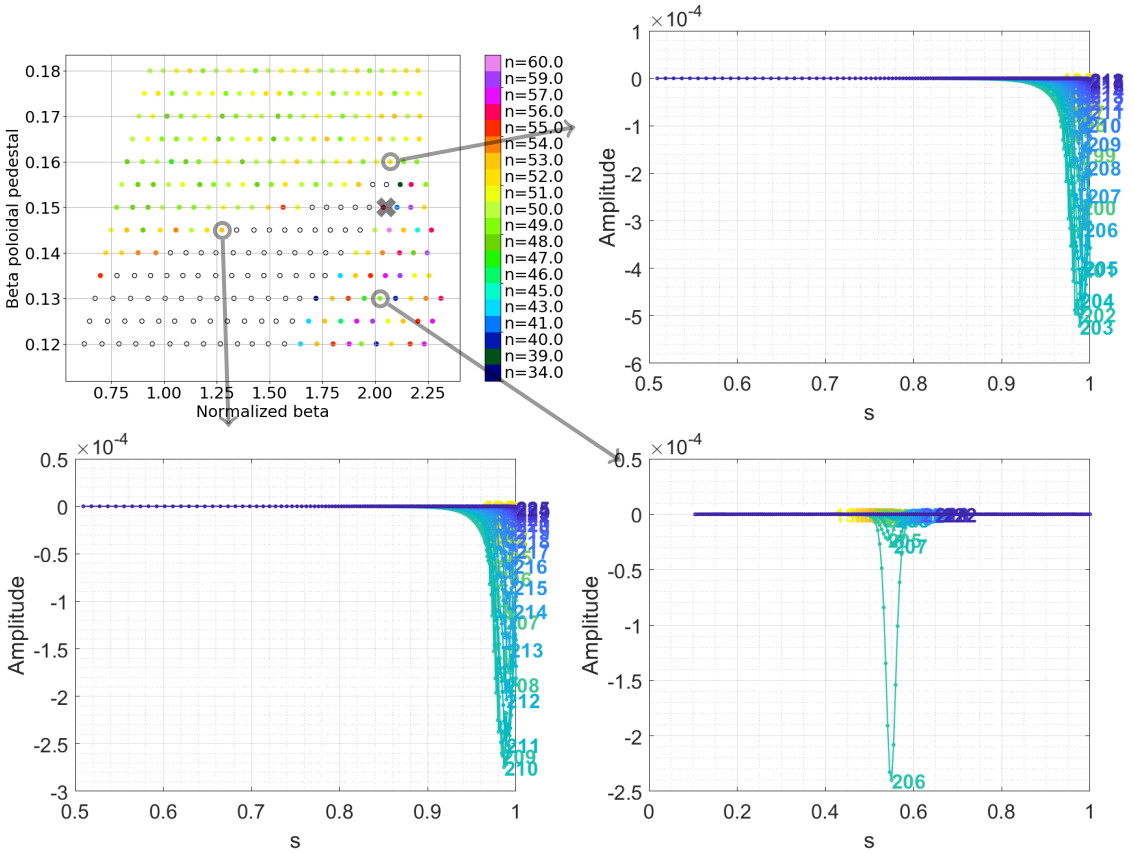

Figure 4.4: Mode structure for three points of the 7.5MA case with constant pedestal width, with also given which point it is in the stability graph from figure 4.5. For these stability calculations the 'fast' mode of MISHKA is used, in which the mode numbers are chosen automatically.

4.3 10MA-5.3T constant pedestal width

For the 10MA case, the large region of n=2 modes stands out, but for lower β_N the mode numbers for the instabilities limiting $\beta_{p,ped}$ are lower for the 10MA case (around n=10) compared to the 15MA case (around n=30). This can be explained through the higher stable $\beta_{p,ped}$, which is a logical result of a lower current with the same magnetic field, which is known to stabilize MHD. Note that this is $\beta_{p,ped}$, not the absolute pressure, which can be seen in section A.2 for the reference case. The higher $\beta_{p,ped}$ results in a relatively higher edge bootstrap current (compared to the core current density), i.e. the fraction of the pedestal current from the total current is much larger. This leads to low-n modes, which is recognized to be the same behavior that is also seen in [36, figure 13]. Here instabilities are shown in a graph where I_{ped}/I_{tot} is plotted versus p_{ped}. The higher I_{ped}/I_{tot} ratio, that is seen for the 10MA scenario, results in the low-n modes.

Because of these $n = 2$ modes, there is a 'plateau' around $\beta_N = 2.0$ in which the maximum stable pedestal height doesn't increase (or at least increases much slower) when changing β_N. This is due to the safety factor, q, which is getting close to a rational number (5.5 in this case), giving unstable modes. For example, the five $n = 2$ modes at $\beta_{p,ped} = 0.20$ have values for the edge safety factors of, from low to high β_N, $q_{95} = 5.37, 5.39, 5.41, 5.42, 5.44$, showing a build-up towards $q = 5.5$, after which stability is again found for larger β_N at the same value of $\beta_{p,ped} = 0.20$. This is because a rational q means that field lines close on themselves so that, when the perturbation is aligned with q there is no field line bending, which is known to be stabilizing, as explained in section 2.2.2. With further increasing β_N, q changes so much that stability can be reached again, so that the stable pedestal height can be increased again. For higher β_N and $\beta_{p,ped}$ an area of $n = 3$ modes can be seen. To go from $n = 2$ to $n = 3$ is a fifty percent increase in toroidal mode number, whereas between higher-n modes this is a relatively smaller step. Therefore, since low-n modes alternate slower, a much larger area of low-n modes can be seen.

All of this is thought to be caused by the small 'wiggle' of reversed global shear at the edge of the q-profile, as can be seen in figure 3.4b, which are known to stabilize high-n ballooning modes [37], so that the low-n modes appear. Another difference is the place of the reference point, which is clearly not limited by the height of the pedestal, but by high β_N (infernal modes). This is because this case was designed to push the limits of ITER, by having high pressure gradients in the core of the plasma. These gradients are present, because the high bootstrap current in the core needs to compensate for the missing inductively driven current, so that steady-state can be reached. More elaborate simulations on this scenario were also done at ITER and there it was seen that it is near the limit of stability. Therefore, although the reference point is even just in the unstable part, here it could also be interpreted as marginally stable.

The mode structures, see figure 4.6, show that modes in the high $\beta_{p,ped}$ region, outside of the $n = 2$ region, in the lower left plot, are peeling-ballooning modes although lower mode numbers than for the 15MA case (around $n = 10$ instead of $n = 30$ in the 15MA case), the mode structure looks very similar. However, when looking at the mode structure of the $n = 2$ modes, in the upper right plot, these show a relatively high amplitude for one mode at the edge. This finite value of current density, especially for one harmonic, is characteristic for a kink-peeling mode, as

was discussed in section 2.2.2. The smaller $n = 3$ region shows similar modes. It is possible that these low-n localized kink-peeling modes lead to a saturated mode, the so-called quiescent H-mode, or QH-mode, in which ELMs are replace with EHOs, edge harmonic oscillations, that shows a similar periodic behavior, but without the devastating outbursts of energy. [31] It must be noted that such low-n kink-peeling modes in general have been found to be sensitive for the value of q at the edge and they might be stable in a real x-point plasma.[38] Therefore in some models, it is chosen that these modes are not taken into account.

Again, the high β_N instabilities are infernal modes, as can be seen in the lower right graph of figure 4.6. These are now a bit wider (looking at the main structure), consisting of more toroidal mode numbers and shifted slightly towards the edge: highest peak around $s = 0.5$ instead of $s = 0.4$, as was the case for the 15MA case. Growth rates are 0.142 for the infernal mode, 0.097 for the low β_N peeling-ballooning mode and 0.0613 for the kink-peeling mode.

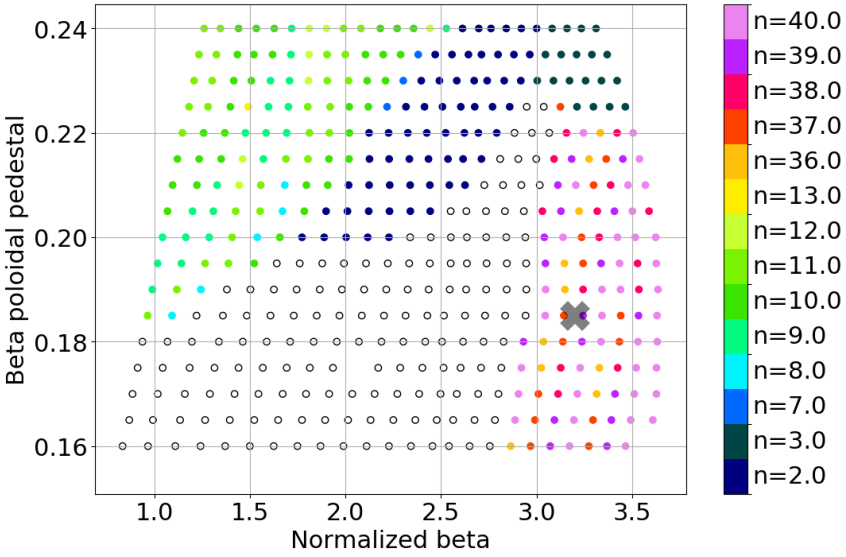

Figure 4.5: Stability graph for the 10MA, 5.3T scenario. $\beta_{p,ped}$ vs β_N, in which for each point the most unstable mode is depicted. Empty circles give stable modes and for the unstable modes, the most unstable toroidal mode number is given by the color. The original ASTRA point is given by the cross. For these stability calculations the 'fast' mode of MISHKA is used, in which the mode numbers are chosen automatically.

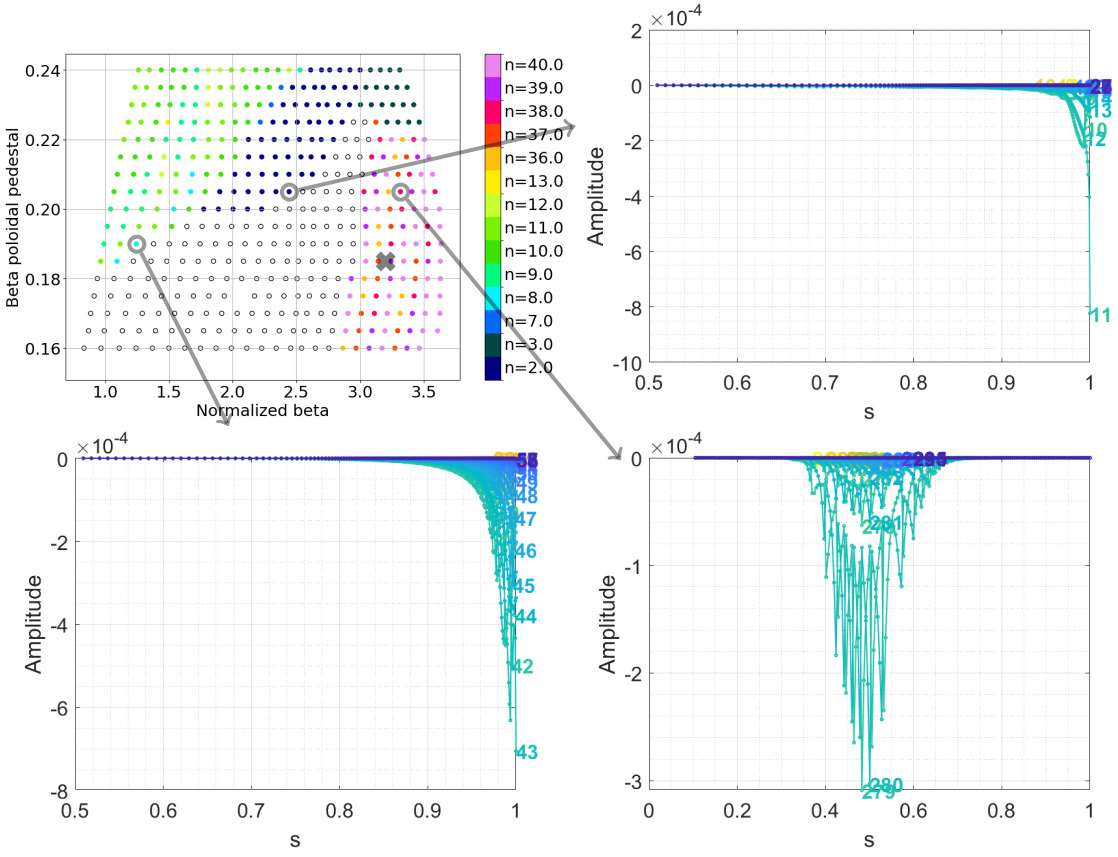

Figure 4.6: Mode structure for three points of the 10MA case with constant pedestal width, with also given which point it is in the stability graph from figure 4.5.

4.4 Varying pedestal width

The pedestal width is then varied according to $\Delta_{\psi_N} \propto \beta_{p,ped}^{1/2}$, so that it is approximately constant in real space. This change in pedestal width in poloidal flux coordinates is a process that has been seen in experiments to happen spontaneously. For these simulations, the ASTRA simulation is used as the reference point to scale the pedestal width.

When compared with the reference case, a lower $\beta_{p,ped}$ than the reference case, would give a lower pedestal width. With the same gradient, this leads to a lower achievable stable pedestal. For a $\beta_{p,ped}$ higher than the reference case, the opposite is true. This gives a wider pedestal, for which the same gradient gives a higher pedestal. Overall, the change in $\beta_{p,ped}$ would then be expected to be bigger for the same change in β_N (lower $\beta_{p,ped}$ for low β_N and higher $\beta_{p,ped}$ for high β_N). This effect can clearly be seen for the 7.5MA and 15MA scenarios. For the 15MA scenario, for basically the same range of β_N, the constant pedestal width gives $\beta_{p,ped} = [0.125, 0.145]$, whereas for the varying pedestal width this is $\beta_{p,ped} = [0.105, 0.16]$. For the 7.5MA scenario, the constant pedestal width gives $\beta_{p,ped} = [0.13, 0.155]$, while for the varying pedestal width there is a range of $\beta_{p,ped} = [0.125, 0.17]$.

However, for the 10MA case this is not seen, as for both a constant and varying pedestal width, the range of pedestal heights is the same: $\beta_{p,ped} = [0.18, 0.225]$. Although slight differences between constant and varying pedestal width are seen (e.g. the plateau is slightly wider), there is not a big difference between the two. It is believed that this is the case because for these kink-peeling modes, it is the gradient at the edge, which doesn't change with changing the width, that is important. For the peeling ballooning modes, on the other hand, it is the integral of this gradient, i.e. the pedestal height, which does change, that is important.

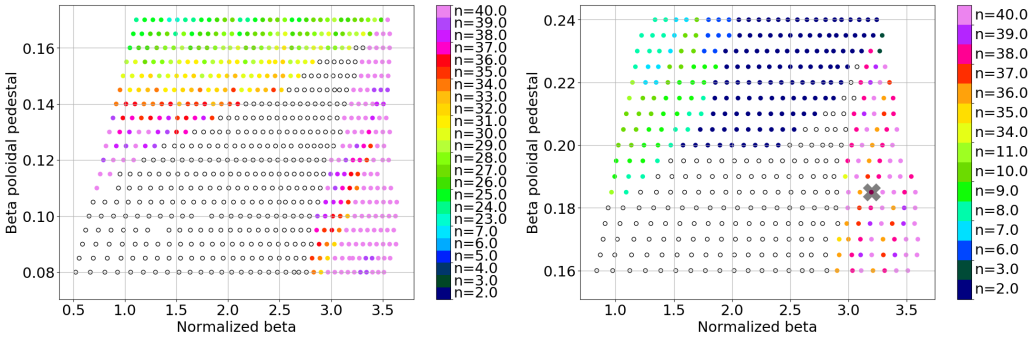

(a) 15MA, 5.3T

(b) 10MA, 5.3T

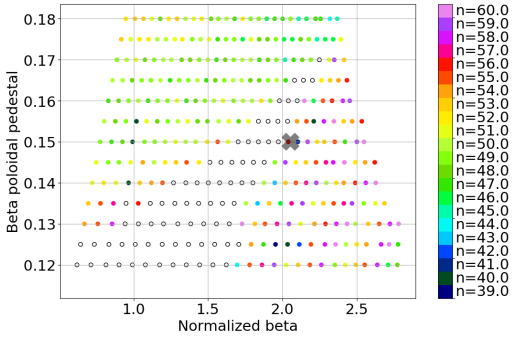

(c) 7.5MA, 2.65T

Figure 4.7: Stability graph for all scenarios, with the pedestal width scaling as $\Delta_p si \propto \beta_{p,ped}^{-1/2}$, normalized to the ASTRA reference cases. $\beta_{p,ped}$ vs β_N is plotted, in which for each point the most unstable mode is depicted. Empty circles give stable modes and for the unstable modes, the most unstable toroidal mode number is given by the color. The original ASTRA point is given by the cross. Note that the axes ranges are not exactly the same.

4.5 Derivation of a relation between pedestal and total pressure from MHD stability graphs

For all scenarios, we can then take the most stable points, only including those for which β_N is large enough to have passed the L-H transition, which is about $\beta_N > 1.5$. This can be calculated from the formula

$$\beta_{N,minHmode} = \beta_{Nref} \left(\frac{P_{L-H}}{P_{ref}} \right)^{0.67}, \tag{4.1}$$

[A. Loarte, private communication], resulting in $\beta_{N,minHmode} \approx 1.57$.

A relation between pedestal and total pressure, in terms of poloidal β, can be derived for both assumptions: either keeping the pedestal width constant (from sections 4.1, 4.2 and 4.3) and or varying the pedestal width with the square root of $\beta_{p,ped}$ (section 4.4), as described in section 3.1.

For all different scenarios, for both constant and varying pedestal width, the most stable points (beyond the L-H transition) are plotted together in figure 4.8. The fit according to equation (2.28), $\beta_{p,ped} \propto \beta_{p,tot}^{\alpha}$, is plotted, with the determined value of α. As mentioned, the higher $\beta_{p,ped}$ for the 10MA case is because of the lower current to magnetic field ratio. The difference between the 15MA and 7.5MA cases exists because of different pressure and current density profiles (with the small $\beta_{p,tot}$ maximum because of off-axis neutral beam heating). This is because different ASTRA reference cases were chosen.

For the inductive scenarios, it is clear that a varying pedestal width gives a stronger relation than a constant pedestal width. For each line, taking only the first and last points the relative increase in both $\beta_{p,tot}$ and $\beta_{p,ped}$ can be calculated and this can be compared. For the 15MA scenario, the constant pedestal width gives a 12% increase in $\beta_{p,ped}$ for an increase by a factor 2 of $\beta_{p,tot}$. For the varying pedestal width there is a similar difference in $\beta_{p,tot}$ by a factor 2.11, but a larger increase of $\beta_{p,ped}$ by 28%. For the reference point, compared to the most left point, which is assumed to be just after the L-H transition, an increase in β_N of 23% gives an increase in $\beta_{p,ped}$ of 8%. For the 7.5MA case, the constant pedestal width gives an increase in $\beta_{p,tot}$ of 42% and an accompanying increase in $\beta_{p,ped}$ of 7%. For a varying pedestal width in this scenario, a 51% increase in $\beta_{p,tot}$ gives an increase in $\beta_{p,ped}$ of 17%. This shows that the (more realistic) assumption of the varying pedestal width, is necessary to make the core-edge feedback mechanism a valuable effect for ITER.

For the 10MA case, firstly, in the fit it can be seen that the power law relation, equation (2.28), is not suitable. Also, it doesn't change when varying the pedestal width. Both effects are related to the nature of the modes that are found, as explained in sections 4.3 and 4.4. It must be noted that the region of $\beta_{p,tot}$ that is achievable for ITER, up to around $\beta_{p,tot} \approx 1.1$ for the 10MA case, is within the region of the plateau. Therefore, in this scenario the core-edge feedback mechanism might only be useful for a small range of $\beta_{p,tot}$ values near at the high end of what is achievable for ITER.

This plateau could also be the saturation of the effect that is (thought to be) found in [1]. However, they didn't find a subsequent rise in $\beta_{p,ped}$ because β_N wasn't increased enough, or that wasn't possible, so that a saturation limit was concluded, instead of the plateau that is seen in this work. This is thus only found for the 10MA

steady-state scenario as no saturation limit (or plateau) is found for the 7.5MA or 15MA inductive scenarios.

The values of α resulting from the fit, can be compared to experiments. In [2, figures 16 and 17], the core energy and the pedestal energy, which are similar definition as $\beta_{p,ped}$ and $\beta_{p,core}$, are looked at separately as function of power. Combining those, values of the power law relation between $\beta_{p,ped}$ and $\beta_{p,core}$ can be found, and for three different scenarios, they are given in table 4.1. These scenarios are: a carbon wall with a high triangularity plasma, an ITER-like wall (ILW) with high triangularity and an ILW with low triangularity. It should be noted that, as mentioned before in chapter 1, due to the experimental conditions the carbon wall experiment represents ITER most. This is because in this experiment, gas puffing is low, so that collisionality is low, which results in a high bootstrap current at the edge of the plasma, as is also the case for ITER. Especially comparing the value of α from this experiment, $\alpha_{Cwall} = 0.412$, to the values of the inductive scenarios with varying pedestal width, $\alpha_{7.5MAvw} = 0.416$ and $\alpha_{15MAvw} = 0.319$, these values are in good agreement.

It must be noted that the experiments described in [2], are hybrid scenario experiments. It could mean that a difference in inductive or hybrid scenario, has no effect on the relation between $\beta_{p,ped}$ and $\beta_{p,tot}$. However, it could also mean that the agreement is just a coincidence that exists because the difference in conditions. Thus, although it seems that simulation of ITER agree with experiments that resemble ITER conditions, not enough research is done to make a thorough comparison between experiments in current devices and the simulations done in this work for ITER.

Table 4.1: Values of α calculated from [2] for three different experiments: a carbon (C) wall, and for an ITER-like wall (ILW) with both a high and low triangularity plasma configuration.

	α from [2]
C-wall high triangularity	0.412
ILW high triangularity	0.788
ILW low triangularity	0.619

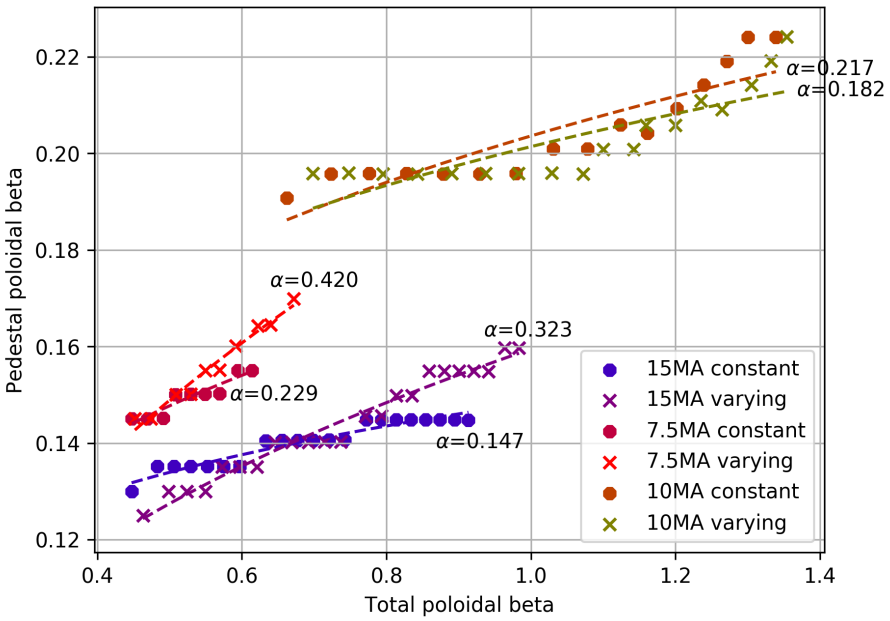

Figure 4.8: For different scenarios, both a simulation with constant and one with varying pedestal width are done. The most stable pedestal heights are taken from figures 4.1, 4.3, 4.5 and 4.7, only for $\beta_{p,tot}$ greater than the L-H threshold. These points are fitted to the relation $\beta_{p,ped} \propto \beta_{p,tot}^{\alpha}$, with α given for all fits.

4.6 Comparison to scaling law

As mentioned before, the IPB98(y,2) gives a scaling law, $\tau_{E,th}^{ELMy} \propto P^{-0.69}$, so that $W = \tau_E \cdot P \propto P^{0.31}$. However, the results from this project only give half of the core-edge feedback mechanism, namely the MHD part, given by equation (2.28). To include the transport part, given by equation (2.29), a value for the stiffness is needed. Since no data about this for ITER is known, different values for the profile stiffness ,δ in equation (2.29), are assumed. Taking the points of the 15MA scenario with varying pedestal width from figure 4.8, an input power, P_{in}, can be calculated through equation (2.34). As explained in section 2.4, the values of $\beta_{p,tot}$ can then be plotted against the calculated P_{in} values and it can be fitted for equation (2.31), however with another γ then the IPB98(y,2) scaling law, thus: $W_{tot} \propto P_{in}^{\gamma_{fit}}$. Note that these cases are normalized on the reference case. The difference in $\beta_{p,tot}$ here and the expected value of $\beta_{p,tot} \approx 0.65$ is because fast particles are not taken into account, which are indeed expected to deliver about ten percent of the total pressure. For each assumption of stiffness δ, this fit can be made and a value for γ_{fit} is obtained. These fits and the values found for γ_{fit} for each δ are given in figure 4.9. This is done for stiffnesses in the range of $\delta = [0.1, 0.6]$. The resulting values of γ_{fit} turn out to give a linear relation with δ:

$$\gamma_{fit} = 1.18\delta. \tag{4.2}$$

Because an expected value of this δ, the stiffness parameter, for ITER is not known, hard conclusions can't be drawn from this. Also it is not possible to extrapolate the value of this stiffness from experimental data, e.g. [2]. However, an interesting value is that for which $\gamma = 0.31$, the IPB98(y,2) value. For that a stiffness of $\delta = 0.263$ is necessary. Another interesting value is for which $\gamma = 0.5$, which, as explained

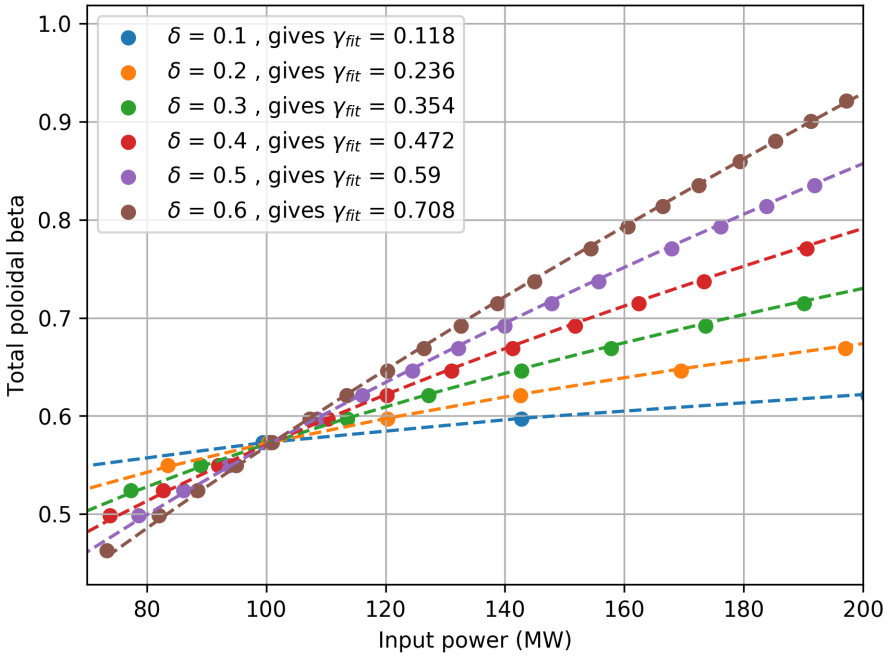

Figure 4.9: Fit through $\beta_{p,tot}$, taken from the point of the 15MA scenario with varying pedestal width, for which $\alpha = 0.32$, in figure 4.8, as function of P_{in}, calculated from equation (2.34), for different assumptions of profile stiffness δ. This results in a γ_{fit} for each δ, from a fit according to $\beta_{pol,tot} \propto P_{in}^{\gamma_{fit}}$.

in section 2.4, is the boundary between a stable and unstable burning plasma. To keep a stable burning plasma, $\delta = 0.424$ is the maximum value of the stiffness that should be obtained.

Even though the stiffness is not exactly known, an estimate can be made of the impact of this effect on confinement. When looking at figure 4.8 again, let's consider the 15MA case with varying pedestal width. The point with the lowest $\beta_{p,tot}$ is assumed to be just after L-H transition. Without any feedback effect, this scenario the pedestal height would be constant at $\beta_{p,ped} \approx 0.125$. To go to the reference case (around $\beta_{p,tot} \approx 0.58$ and $\beta_{p,ped} \approx 0.135$, it would be an increase of 8%. Moreover, when enough power would be available to use the effect all the way up to global instability, and increase of 28% could be reached. Since it can be assumed that the pedestal carries about half of the energy of the plasma, confinement increases only by half of this. This estimate would thus give an increase of 4-14% of confinement due to the core-edge positive feedback mechanism. This is thus dependent on the amount of heating power available, and the total effect of course also depends on core confinement.

Chapter 5

Conclusions and future work

A comprehensive model using axisymmetric ideal MHD equilibrium code HELENA and stability code MISHKA is created, in order to research the positive feedback mechanism between core pressure and edge stability in ITER. This feedback mechanism was found to have limits in other devices, but that was not found in the scenarios that are researched for ITER.

There are two sides to this feedback mechanism: MHD, through Shafranvo shift, and transport, through profile stiffnes. The MHD part is researched numerically. MHD simulations are done for different scenarios: two inductive scenarios (15MA/5.3T and 7.5MA/2.65T) and one steady-state scenario (10MA/5.3T). For all of these, firstly a constant pedestal width was assumed, after which the model was refined to take into account a pedestal width varying according to the EPED model [34].

For the inductive scenarios the maximum attainable pedestal height is limited by peeling-ballooning modes. For the beneficiary effect on the pedestal height by increasing total pressure no saturation limit to the pedestal height is found. However, the effect is eventually limited by infernal modes in the core of the plasma for large β_N, which lead to disruptions. In both inductive cases, however, the strength of the effect is only practically valuable if the pedestal width is scaled more realistically to the pedestal height, rather than keeping it constant. Therefore the varying of the width is shown to be a necessary refinement in this model.

In the steady-state scenario the maximum attainable pedestal height is limited by low-n kink-peeling instabilities, at much higher values of $\beta_{p,ped}$, compared to the inductive scenarios. A clear saturation limit is not found here either, but in the range of $\beta_{p,tot}$ that ITER operates in, there is a plateau for which the pedestal height is constant for a range of $\beta_{p,tot}$. This plateau is possibly the apparent saturation limit that was found in [1].

Comparison with experimental results from JET [2] shows good agreement of the inductive scenarios in which the pedestal width is varied, with the experiment that is most resemblant to ITER conditions. It might be possible that experimental results from current devices are a good estimate for ITER, although more research is needed to confirm this.

The other side of the feedback mechanism is determined by transport. Since no values of profile stiffness are known for ITER, these are assumed theoretically. Using this, two interesting values of the stiffness are looked at. In order to obey the IPB98(y,2) ITER scaling law, a value for the stiffness of $\delta = 0.263$ is determined to

be necessary. Furthermore, to keep a stable burning plasma, a stiffness of $\delta \leq 0.424$ is found to be needed.

Only looking at the MHD results, gives an estimate of the increase in confinement that can be obtained through the feedback mechanism in ITER. An increase of 4-14% in confinement is estimated, which depends on the available heating power. Also, not knowing the exact details of core confinement gives an uncertainty here.

Although a lot of information can be taken from this research, further research is required. Especially for the steady-state scenario, it should be looked at whether this plateau still exists for simulations using more sophisticated theories than ideal MHD. These can include resistive MHD, with a finite resistance, or extended MHD, taking higher order effect into account that can be described by a single fluid.

Also other cases can be investigated such as, for example, a lower triangularity case since it was seen it has a definite impact. Also, a hybrid scenario could be chosen. When this is done, a further comparison with [2] can be made. Furthermore, other plasma parameters can be studied and the framework developed in this graduation project can be applied to other tokamaks, so that direct comparison with experiments becomes a possibility.

Finally, another thing that is found experimentally is that the position of the maximal gradient in the pedestal can shift outward, which is especially seen when Tungsten is present [39]. This is an effect that could be added to the model.

It was shown with this comprehensive model that the effect of the core-edge feedback mechanism differs within ITER operational space. The interesting results from this work shows some details about ITER operation. Combining this with future research will help going towards the development of ITER and fusion energy on earth.

List of Figures

1.1 H-mode pressure profile . . . 3
1.2 Poloidal cross section . . . 3
1.3 Saturation limit of feedback mechanism . . . 6
1.4 Pressure, core and total energy as function of power from [2] . . . 6

2.1 Validity of ideal MHD . . . 9
2.2 Stability and instability . . . 10
2.4 Schematic representation of Shafranov shift . . . 16

3.1 Pressure profile changes through HELENA parameters . . . 20
3.2 Bootstrap current adaptation . . . 21
3.4 Normalized safety factor, pressure and current density profiles . . . 23
3.3 ITER plasma geometry . . . 24

4.1 15MA/5.3T stability graph . . . 29
4.2 15MA/5.3T constant pedestal width mode structures for some modes 29
4.3 7.5MA/2.65T stability graph . . . 31
4.4 7.5MA/2.65T constant pedestal width mode structures for some modes 31
4.5 10MA/5.3T stability graph . . . 34
4.6 10MA/5.3T constant pedestal width mode structures for some modes 34
4.7 Varying pedestal width stability graphs . . . 36
4.8 Fitting of $\beta_{p,ped}$ as function of $\beta_{p,tot}$ to determine α . . . 39
4.9 Fit to determine γ from different assumption of stiffness δ . . . 40

A.1 15MA/5.3T constant pedestal width 2D mode structures . . . 50
A.2 7.5MA/2.65T constant pedestal width mode structures for some modes 51
A.3 10MA/5.3T constant pedestal width 2D mode structures . . . 52
A.4 Non-normalized pressure and current density profiles . . . 53

List of Tables

4.1 Comparison of α values with Challis paper [2] . . . 38

Bibliography

[1] E Wolfrum, M Beurskens, MG Dunne, L Frassinetti, X Gao, C Giroud, J Hughes, T Lunt, R Maingi, T Osborne, et al. Impact of wall materials and seeding gases on the pedestal and on core plasma performance. *Nuclear Materials and Energy*, 2017.

[2] Clive D Challis, J Garcia, M Beurskens, P Buratti, E Delabie, P Drewelow, Lorenzo Frassinetti, C Giroud, N Hawkes, J Hobirk, et al. Improved confinement in jet high β plasmas with an iter-like wall. *Nuclear Fusion*, 55(5):053031, 2015.

[3] EDA ITER et al. Plasma confinement and transport. *Nuclear Fusion*, 39(12 ITER physics basis):2175–2249, 1999.

[4] Hannah Ritchie. How long before we run out of fossil fuels? 08-08-2017. Accessed: 05-02-2018.

[5] Laurence O Williams. *An end to global warming*. Gulf Professional Publishing, 2002.

[6] ITER - Fueling the fusion reactor. https://www.iter.org/sci/FusionFuels. Accessed: 16-01-2018.

[7] EUROfusion - 50 years of tokamaks. https://www.euro-fusion.org/newsletter/50-years-of-tokamaks/. Accessed: 16-01-2018.

[8] ITER - How Fritz Wagner "discovered" the H-Mode. https://www.iter.org/newsline/86/659. Accessed: 16-01-2018.

[9] RD Smirnov, A Yu Pigarov, M Rosenberg, SI Krasheninnikov, and DA Mendis. Modelling of dynamics and transport of carbon dust particles in tokamaks. *Plasma Physics and Controlled Fusion*, 49(4):347, 2007.

[10] W Fundamenski, Volker Naulin, T Neukirch, Odd Erik Garcia, and J Juul Rasmussen. On the relationship between elm filaments and solar flares. *Plasma Physics and Controlled Fusion*, 49(5):R43, 2007.

[11] ELMs – friend or foe? https://www.euro-fusion.org/2013/08/elms/. Accessed: 05-02-2018.

[12] PB Snyder, HR Wilson, JR Ferron, LL Lao, AW Leonard, D Mossessian, M Murakami, TH Osborne, AD Turnbull, and XQ Xu. Elms and constraints on the H-mode pedestal: peeling–ballooning stability calculation and comparison with experiment. *Nuclear fusion*, 44(2):320, 2004.

[13] Peter Alan Davidson. *An introduction to magnetohydrodynamics*, volume 25. Cambridge university press, 2001.

[14] Jeffrey P Freidberg. Ideal magnetohydrodynamics. 1987.

[15] Nick Murphy. Ideal MHD - Harvard-Smithsonian Center for Astrophysics. https://www.cfa.harvard.edu/~namurphy/Lectures/Ay253_01_IdealMHD.pdf, February 1, 2016. Accessed: 19-01-2018.

[16] Jeffrey P Freidberg. Ideal magnetohydrodynamic theory of magnetic fusion systems. *Reviews of Modern Physics*, 54(3):801, 1982.

[17] On equilibrium, spherical cows and notes for tougher times. https://medium.com/hopes-and-dreams-for-our-future/on-equilibrium-spherical-cows-and-notes-for-tougher-times-224a1296f16d. Accessed: 19-01-2018.

[18] Ira B Bernstein, EA Frieman, Martin David Kruskal, and RM Kulsrud. An energy principle for hydromagnetic stability problems. In *Proc. R. Soc. Lond. A*, volume 244, pages 17–40. The Royal Society, 1958.

[19] Kiran Chandra Das. On stationary values of rayleigh quotient of an operator. *Journal of Mathematical Analysis and Applications*, 48(2):527–533, 1974.

[20] T Weyens. 3D ideal linear peeling ballooning theory in magnetic fusion devices. 2017.

[21] John M Greene and John L Johnson. Interchange instabilities in ideal hydromagnetic theory. *Plasma Physics*, 10(8):729, 1968.

[22] PB Snyder, HR Wilson, and XQ Xu. Progress in the peeling-ballooning model of edge localized modes: Numerical studies of nonlinear dynamics. *Physics of Plasmas*, 12(5):056115, 2005.

[23] D Dobrott, DB Nelson, JM Greene, AH Glasser, MS Chance, and EA Frieman. Theory of ballooning modes in tokamaks with finite shear. *Physical Review Letters*, 39(15):943, 1977.

[24] GTA Huysmans. Elms: Mhd instabilities at the transport barrier. *Plasma Physics and Controlled Fusion*, 47(12B):B165, 2005.

[25] HR Wilson, PB Snyder, GTA Huysmans, and RL Miller. Numerical studies of edge localized instabilities in tokamaks. *Physics of Plasmas*, 9(4):1277–1286, 2002.

[26] A Kleiner, JP Graves, D Brunetti, WA Cooper, FD Halpern, J-F Luciani, and H Lütjens. Neoclassical tearing mode seeding by coupling with infernal modes in low-shear tokamaks. *Nuclear Fusion*, 56(9):092007, 2016.

[27] Gerardus Titus Arnoldus Huijsmans, Promotor Prof Dr Ir JP Goed, et al. *External resistive modes in tokamaks*. PhD thesis, [Amsterdam]: Vrije Universiteit, 1991.

[28] AB Mikhailovskii, GTA Huysmans, WOK Kerner, and SE Sharapov. Optimization of computational mhd normal-mode analysis for tokamaks. *Plasma Physics Reports*, 23(10):844–857, 1997.

[29] Dalton D Schnack. *Lectures in magnetohydrodynamics: with an appendix on extended MHD*, volume 780. Springer, 2009.

[30] PB Snyder, HR Wilson, JR Ferron, LL Lao, AW Leonard, D Mossessian, M Murakami, TH Osborne, AD Turnbull, and XQ Xu. ELMs and constraints on the H-mode pedestal: peeling–ballooning stability calculation and comparison with experiment. *Nuclear fusion*, 44(2):320, 2004.

[31] PB Snyder, KH Burrell, HR Wilson, MS Chu, ME Fenstermacher, AW Leonard, RA Moyer, TH Osborne, M Umansky, WP West, et al. Stability and dynamics of the edge pedestal in the low collisionality regime: physics mechanisms for steady-state elm-free operation. *Nuclear Fusion*, 47(8):961, 2007.

[32] PB Snyder, RJ Groebner, AW Leonard, TH Osborne, and HR Wilson. Development and validation of a predictive model for the pedestal height. *Physics of Plasmas*, 16(5):056118, 2009.

[33] Olivier Sauter, Clemente Angioni, and YR Lin-Liu. Neoclassical conductivity and bootstrap current formulas for general axisymmetric equilibria and arbitrary collisionality regime. *Physics of Plasmas*, 6(7):2834–2839, 1999.

[34] PB Snyder, RJ Groebner, JW Hughes, TH Osborne, M Beurskens, AW Leonard, HR Wilson, and XQ Xu. A first-principles predictive model of the pedestal height and width: development, testing and iter optimization with the eped model. *Nuclear Fusion*, 51(10):103016, 2011.

[35] EJ Strait. Stability of high beta tokamak plasmas. *Physics of Plasmas*, 1(5):1415–1431, 1994.

[36] P Maget, J-F Artaud, M Bécoulet, T Casper, J Faustin, J Garcia, GTA Huijsmans, A Loarte, and G Saibene. Mhd stability of the pedestal in iter scenarios. *Nuclear Fusion*, 53(9):093011, 2013.

[37] JF Drake, YT Lau, PN Guzdar, AB Hassam, SV Novakovski, B Rogers, and A Zeiler. Local negative shear and the formation of transport barriers. *Physical review letters*, 77(3):494, 1996.

[38] GTA Huysmans. External kink (peeling) modes in x-point geometry. *Plasma physics and controlled fusion*, 47(12):2107, 2005.

[39] MG Dunne, S Potzel, F Reimold, M Wischmeier, E Wolfrum, Lorenzo Frassinetti, M Beurskens, P Bilkova, M Cavedon, R Fischer, et al. The role of the density profile in the asdex-upgrade pedestal structure. *Plasma Physics and Controlled Fusion*, 59(1):014017, 2016.

Appendix A

Additional graphs

A.1 Mode structures

The 2D mode structure are given for the edge modes, for the three different scenarios, for a constant pedestal width. For the peeling-ballooning modes it shows that modes are also localized at the high field side, although they are larger at the small field side, typical for a peeling-ballooning mode.

A.1.1 15MA-5.3T

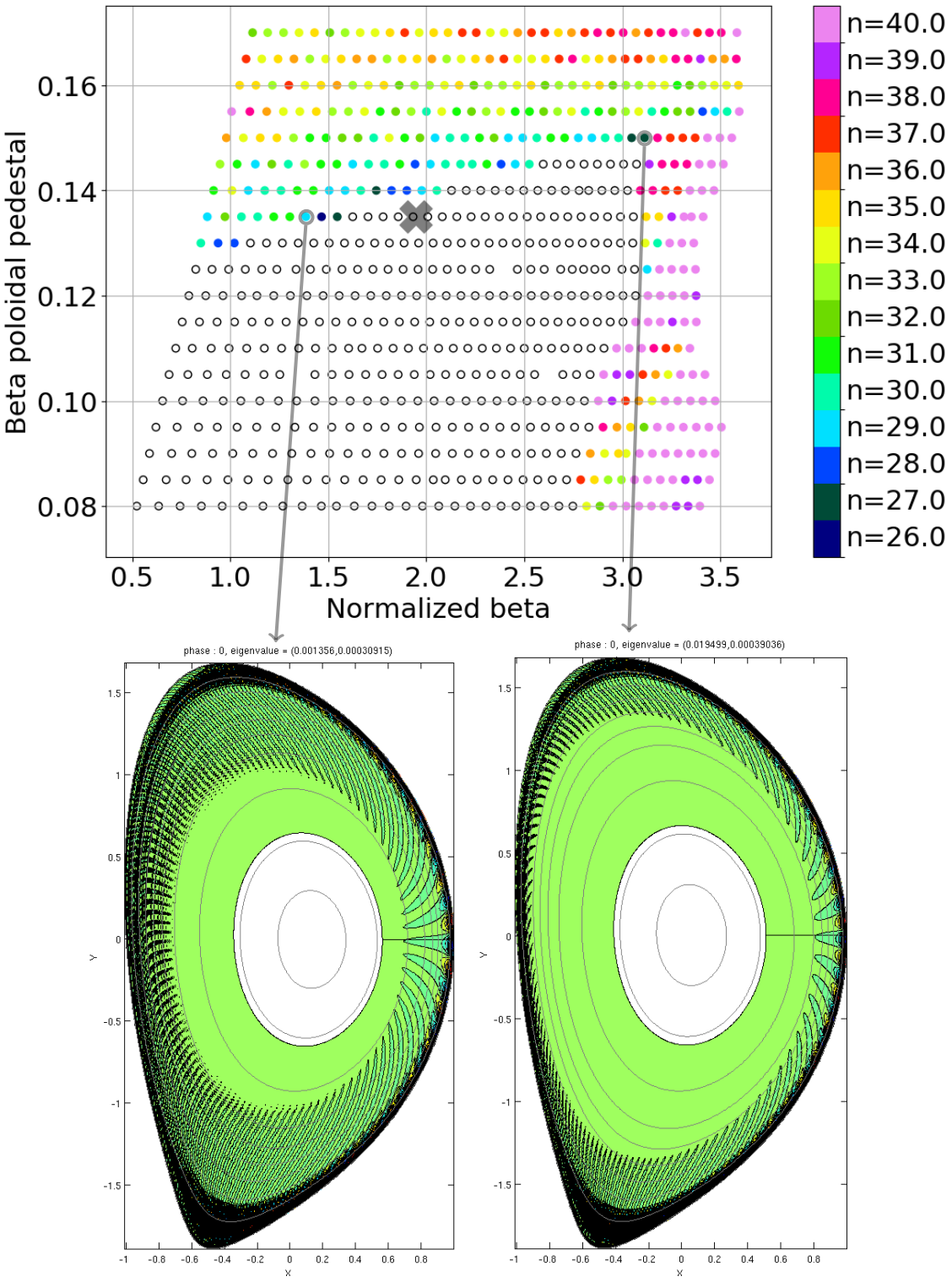

Figure A.1: 2D Mode structure for the 15MA case with constant pedestal width, with also given which point it is in the stability graph from figure 4.1.

A.1.2 7.5MA-2.65T

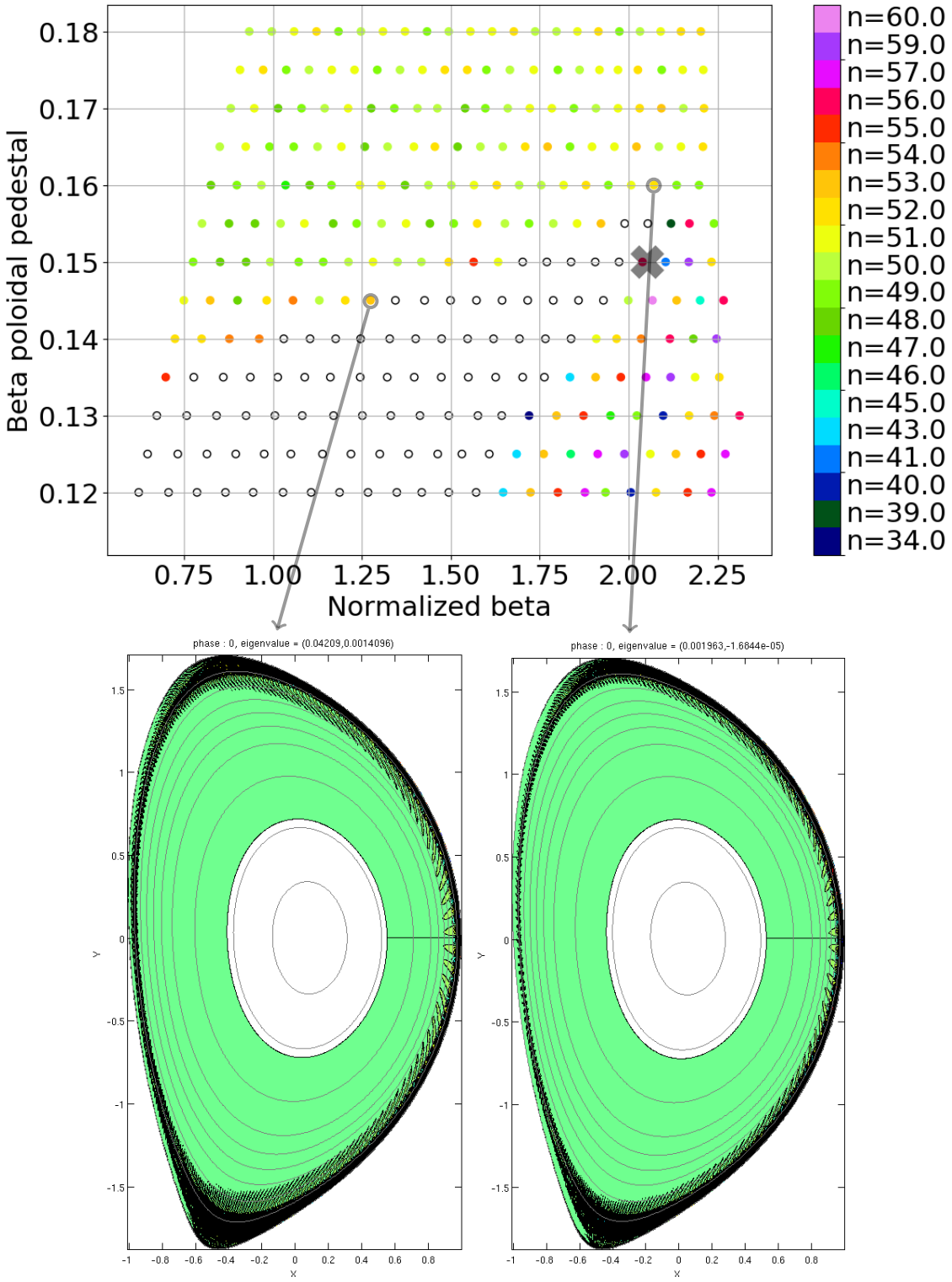

Figure A.2: 2D Mode structure for three points of the 7.5MA case with constant pedestal width, with also given which point it is in the stability graph from figure 4.5.

A.1.3 10MA-5.3T

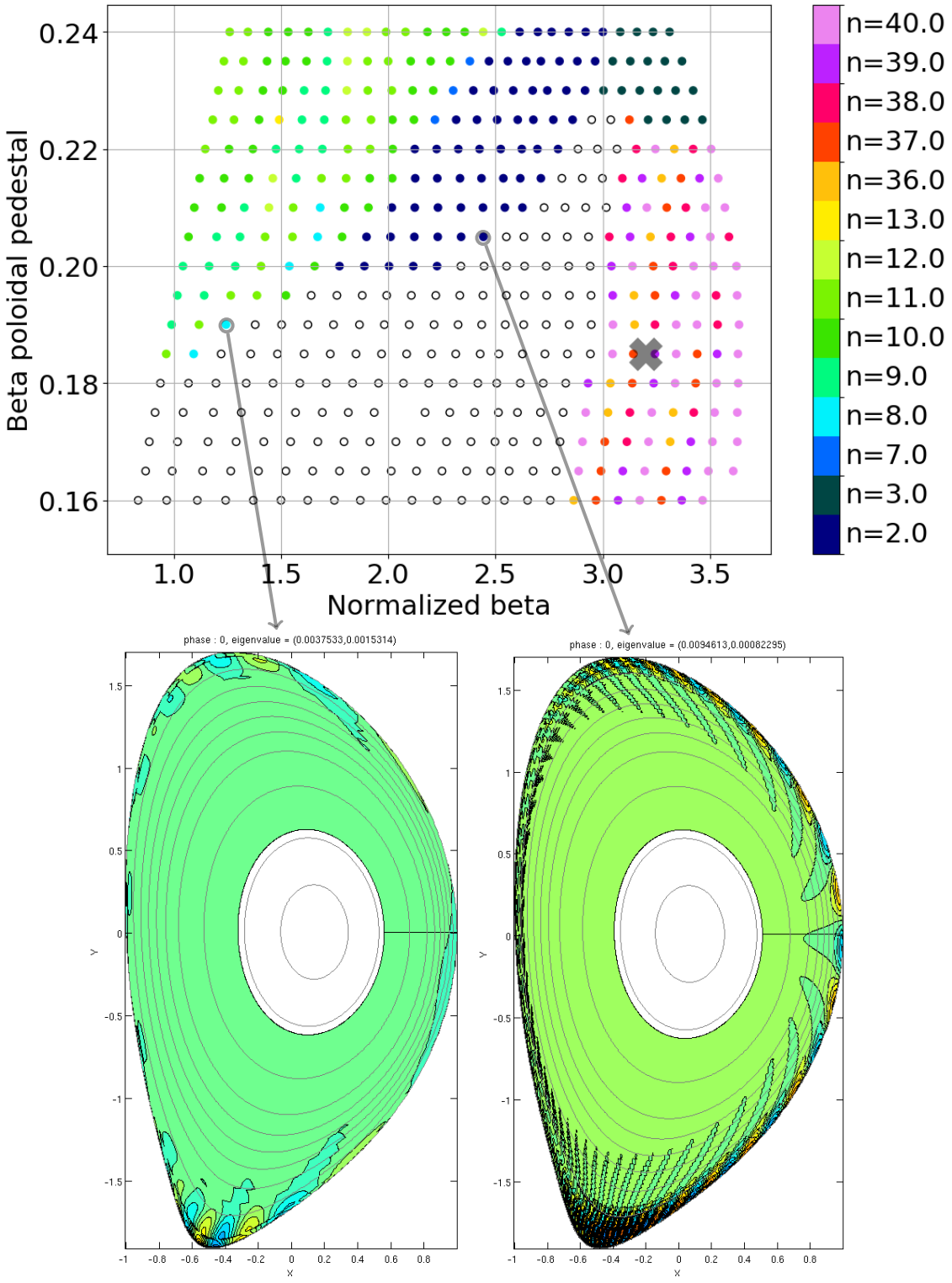

Figure A.3: 2D mode structure for two edge modes of the 10MA case with constant pedestal width, with also given which point it is in the stability graph from figure 4.5.

A.2 Non-normalized current density and pressure profiles

In figure A.4, the current density and pressure profiles are shown that were also shown in figure 3.4 are here given without normalization, so that real values are shown.

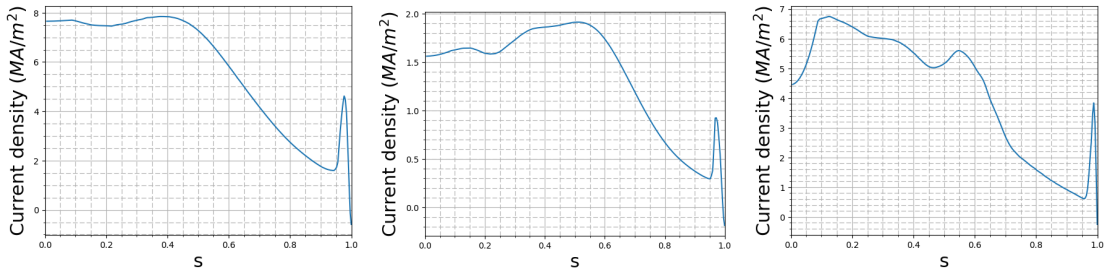

(a) Current density profile for 15MA/5.3T case.

(b) Current density profile for 7.5MA/2.65T case.

(c) Current density profile for 10MA/5.3T case.

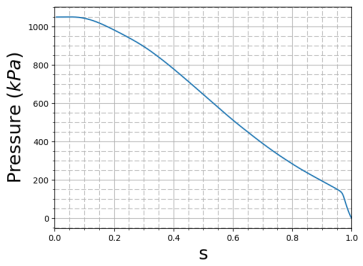

(d) Pressure profile for 15MA/5.3T case.

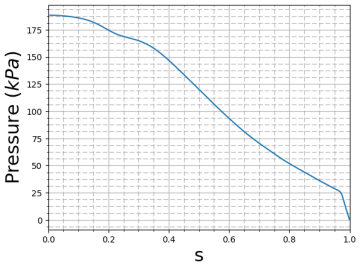

(e) Pressure profile for 7.5MA/2.65T case.

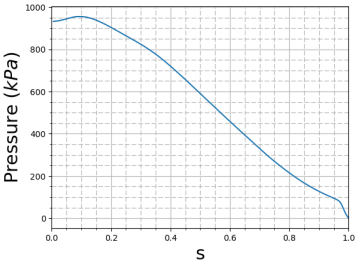

(f) Pressure profile for 10MA/5.3T case.

Figure A.4: Current density and pressure profile for all three scenarios with real values on axes.

Appendix B

EPS conference

B.1 Poster

The poster as was presented on the EPS conference is shown on the next page.

Evaluation of core beta effects on pedestal MHD stability in ITER and consequences for energy confinement

W. Oosterbeek[1], T. Weyens[2], A. Loarte[2], G.T.A. Huijsmans[1,3], F.J. Artola[2,4], A. Polevoi[2], S.H. Kim[2]

[1] *Eindhoven University of Technology, Eindhoven, The Netherlands*
[2] *ITER Organisation, Route de Vinon sur Verdon, CS 90 046, 13067 St Paul Lez Durance Cedex, France*
[3] *CEA, IRFM, F-13108 Saint-Paul-lez-Durance, France*
[4] *Aix-Marseille Université, CNRS, PIIM UMR 7345, 13397 Marseille, France*

Introduction

- Positive feedback mechanism between core and edge
  - MHD: $\beta_{ped} = f(\beta_{core})$ Shafranov shift
  - Transport: $\beta_{core} = g(\beta_{ped})$ Profile stiffness
- Saturation of pedestal height for high β_N in ASDEX-Upgrade [1]
- JET experiments done to investigate core and edge separately
- Is this positive feedback expected in ITER, will there be saturation ?

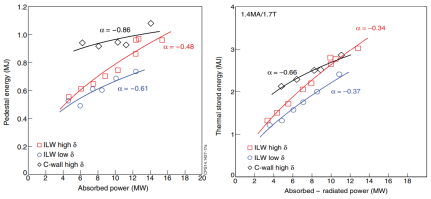

Figure 2. *Pedestal energy (left) and total energy (right) separately as a function of the absorbed power, with α defined by* $E \propto P_{abs}^{\alpha+1}$. *[2,fig.17, JET]*

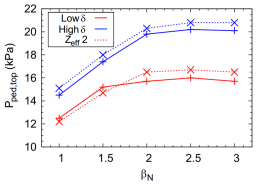

Figure 1. *For low* β_N *, the pedestal height increases with* β_N *, but for high* β_N *this effect is limited: the pedestal height does not increase with* β_N *anymore. [1, fig.1, ASDEX-Upgrade]*

Table 1. *Calculation of values of α from [2], with* $E \propto P^{\alpha}$, *to compare with MHD results.*

	α_{tot}	α_{ped}	α_{MHD}
C-wall high tria.	0.34	0.14	0.412
ILW high tria.	0.66	0.52	0.788
ILW low tria.	0.63	0.39	0.619

2. Model

- Ideal MHD → different pressure profiles → simulate edge stability
- Defining β_{ped} and β_{core} so that $\beta_{poloidal} = \beta_{tot} = \beta_{ped} + \beta_{core}$ → vary core and edge separately
- Numerical:
  - HELENA: 2D Grad-Shafranov equation for equilibrium
  - MISHKA: stability
- Reference case from ASTRA-CORSICA simulations
- Adaptation
  - Pressure profile in HELENA
    - Pedestal width can be varied: $\Delta_{\psi_N} \propto \beta_{ped}^{1/2}$
  - Bootstrap current in HELENA realistically scaled
  - Take only $s = \sqrt{\psi} > 0.5$ in MISHKA → exclude core modes
- Scan over $\{\beta_N, \beta_{ped}\}$ → highest stable pedestals
- Relation between β_{ped} and β_{tot} deduced
  - Assume power law: $\beta_{ped} \propto \beta_{tot}^{\alpha}$
  - α determined through fit
- Comparison with IPB98(y,2) scaling law: $W_{tot} \propto P^{0.31}$
  - Assume profile stiffness: $\frac{\beta_{p,core}}{\beta_{p,ped}} \propto P^{\delta}$
  - Input powers calculated → deduce relation between $\beta_{p,tot}$ and input power
    - $\beta_{p,tot} \propto P^{\gamma}$, with γ determined by another fit

3. 15MA / 5.3T Q = 10

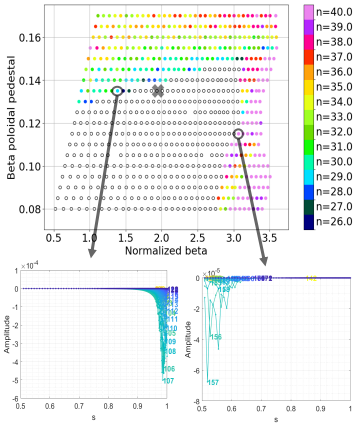

- Results of EPED model → ASTRA reference at stability boundary
- High β_{ped} limited through edge instabilities
  - Peeling-ballooning modes
- high β_N limited through core instabilities
  - Infernal modes.

Figure 3. *Simulations of pedestal beta as function of total beta with different pressure profiles. For every point n=[2,40] are all simulated, and the most unstable modes are plotted in the upper graph, in which the colour gives the mode number and open circles are stable. The black cross is the reference point from ASTRA. The lower graphs are examples of modes, with lower left a peeling-ballooning mode and lower right an infernal mode.*

4. 7.5 MA / 2.65 T

- Similar to 15MA (scaled with I_p^2) but different core profiles
- Unstable at lower β_N; off-axis NBI heating with large CD
  - Wide region of low shear with high pressure gradient

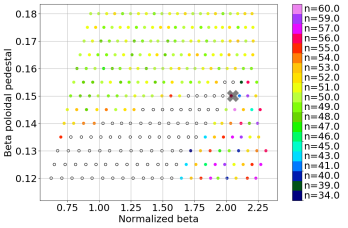

Figure 4. *Graph with stable and unstable equilibria for different pressure profiles, similar to fig. 3 for 7.5 MA/ 2.65 plasma. The black cross is the reference point from ASTRA.*

5. Steady-state 10MA / 5.3T Q = 5

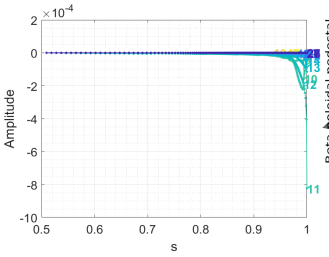

Figure 5. *Mode structure of one of the n=2 kink-peeling modes. One mode clearly gives a high value at the edge, so that it can be distinguished as a kink-peeling mode.*

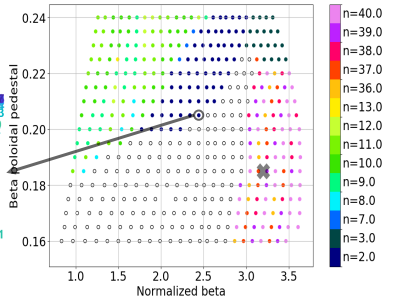

Figure 6. *Graph with stable and unstable equilibria for different pressure profiles, similar to fig. 3, although with a different ASTRA reference case (black cross), the 10MA/5.3T steady-state case.*

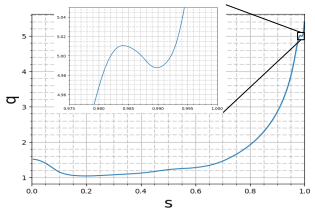

Figure 7. *q-profile of the steady-state case, showing the region of negative global shear at the edge.*

- Lower current with same magnetic field → higher attainable β_{ped}
- Reference case designed for high β_N.
- Much lower toroidal mode numbers → big n=2 region of kink-peeling modes
- Negative global shear near the edge → likely to stabilize high-n modes.
- Plateau because n=2 to n=3 is 50% increase, whereas this is relatively much less for high-n modes.

6. Results

- MHD simulations → $\beta_{ped} \propto \beta_{tot}^{\alpha}$
  - Both for constant and varying pedestal width
  - Take highest stable pedestals
  - Only H-modes studied → $\beta_N \geq 1.5$
  - Fit through these points to determine α
- 7.5MA and 15MA cases
  - Very similar; feedback mechanism found and power law relation is a good assumption
  - Effect of varying width very important for strong core-edge feedback mechanism
  - No saturation limit found up to $\beta_{tot} \sim 1$ (much higher than $\beta_{tot} \sim$ 0.6-0.7 required for Q =10)
- 10MA steady-state
  - A plateau exists in which β_{ped} is constant in a large range of β_{tot}
  - Caused by kink modes
  - ITER steady-state scenario $\beta_{tot} \approx 1.2$, which is in the region of the plateau
  - No hard saturation limit, but β_{ped} does not dependent on β_{tot} in the operational space of ITER
  - Varying width doesn't result in significant changes for 10MA case

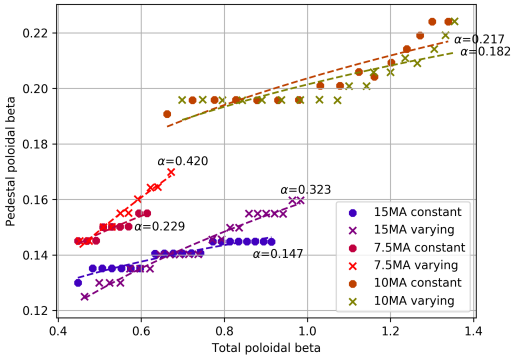

Table 2. *Values from [1] for α to compare with figure 8.*

Challis comparison	α
C-wall high triangularity	0.412
ILW high triangularity	0.788
ILW low triangularity	0.619

- Comparison to JET [2]
- ITER 15 MA and 7.5 MA plasmas with varying pedestal width are close to JET high triangularity with carbon wall → JET with high pedestal pressure and high bootstrap current with low gas fuelling.

Figure 8. *Combination of highest stable pedestal as a function of* β_{tot} *, and fitted to* $\beta_{ped} \propto \beta_{tot}^{\alpha}$ *, with* α *the parameter resulting from that fit.*

- Assume range of stiffness values
- Deduced: $\gamma = 1.18\delta$
- Comparison to IPB98(y,2), $\gamma = 0.31$
  - $\delta = 0.263$
- Comparison $\tau_E \propto \beta_{tot}^2 \propto P_{in}^{2\gamma}$, $\gamma = 0.5$ gives linear relation
  - $\delta = 0.424$

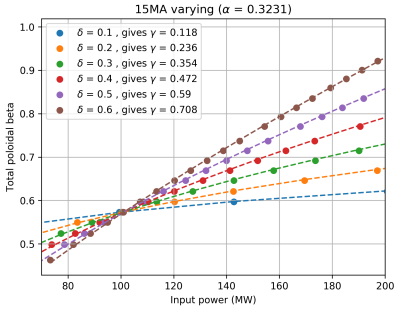

Figure 9. *By combination of MHD and stiffness relations (δ), the power input for every point from fig. 8 can be calculated. This is done for the 15MA case with varying pedestal width (*$\alpha = 0.3231$*). Taking stiffness values in* $\delta = [0.1 - 2.0]$*, for every value a fit to* $\beta_{p,tot} \propto P^{\gamma}$ *is made, and different values of γ for assumptions of δ are given.*

7. Summary

- Feedback mechanism between core and edge studied for ITER
- Three different ITER plasmas 15 MA/5.3 T Q = 10, 7.5 MA / 2.65 T and 10 MA / 5.3 T Q = 5
- No saturation of β_{ped} with β_N has been identified limit but relation varies strongly with plasma scenario
- 15MA and 7.5MA $\beta_{ped} \sim \beta_N^{0.2 - 0.4}$
  - Varying pedestal width as function of β_{ped} maximizes feedback loop
  - ITER results similar to JET carbon wall with high triangularity
- 10MA
  - Low-n kink-peeling modes limit β_{ped}
    - β_{ped} independent of β_N up to $\beta_N \approx 2.7$ (near ITER operational conditions)
    - No influence of varying pedestal width
- Power degradation of confinement for ITER 15 MA/5.3 T plasmas evaluated as a function of core stiffness (δ)

[1] Wolfrum, E., et al. "Impact of wall materials and seeding gases on the pedestal and on core plasma performance." Nuclear Materials and Energy (2017).
[2] Challis, C.D., et al. "Improved confinement in JET high β plasmas with an ITER-like wall." Nuclear Fusion 55.5 (2015): 053031.

45th European Physical Society Conference on Plasma Physics, 2–6 July 2018, Prague, Czech Republic
W. Oosterbeek, Eindhoven University of Technology
Evaluation of core beta effects on pedestal MHD stability in ITER and consequences for energy confinement

Technische Universiteit Eindhoven University of Technology

iter china eu india japan korea russia usa

B.2 four page paper

The 4-page paper is given in the next four pages.

Evaluation of core beta effects on pedestal MHD stability in ITER and consequences for energy confinement

W. Oosterbeek[1], T. Weyens[2], A. Loarte[2], G.T.A. Huijsmans[1,3], F.J. Artola[2,4], A. Polevoi[2], S.H Kim[2]

[1] *Eindhoven University of Technology, Eindhoven, The Netherlands* — [2] *ITER Organization, 13067 St. Paul Lez Durance, France* — [3] *CEA, IRFM, 13108 St. Paul Lez Durance, France* — [4] *Aix-Marseille Université, CNRS, PIIM UMR 7345, 13397 Marseille, France*

Abstract

The maximum stable pedestal pressure has been shown to increase with core pressure and in combination with profile stiffness this can lead to a positive feedback mechanism. However, the effect is shown to saturate for high β in ASDEX-Upgrade [1]. This paper investigates whether this effect appears in ITER scenarios, using ideal MHD numerical codes HELENA and MISHKA for different ITER scenarios from inductive 7.5-15 MA plasmas to steady-state scenarios at 10 MA. No pedestal pressure saturation is found for inductive scenarios; on the contrary for the 10MA steady-state scenario the pedestal pressure is the same for a wide range of total β and is limited by low n kink-peeling modes. Finally, a comparison of the achievable pressure for various levels of core profile stiffness is made with the IPB98(y,2) scaling law.

Introduction

To achieve the ITER fusion production goals it is essential to achieve high energy confinement plasmas (H-mode). Ideal MHD studies of the pedestal stability have shown that the maximum stable pedestal pressure increases with more peaked core pressure profiles due to the Shafranov shift [1]. On the other hand, because of profile stiffness a higher pedestal pressure results in a larger core pressure and higher plasma energy; i.e. a positive feedback mechanism. This effect is shown to have a saturation limit in some cases (e.g. ASDEX-Upgrade [1]), so that extrapolations from current devices, such as JET, [2] may not necessarily be applicable to ITER.

Model

In order to describe this core-edge feedback mechanism, the plasma poloidal beta, β_{tot}, is split into two components: the poloidal pedestal beta, β_{ped} which considers the pedestal, and the poloidal core beta, β_{core} for the core plasma. In this paper we investage the relation between β_{ped} and β_{tot}, which is assumed to be a power law dependence:

$$\beta_{ped} \propto \beta_{tot}^{\alpha}. \tag{1}$$

The stiffness of the core pressure profile is represented by a another power law, in which the ratio of core and pedestal is related to the input power:

$$\frac{\beta_{core}}{\beta_{ped}} \propto P_{in}^{\delta} \tag{2}$$

with P_{in} the input power and δ a measure for the stiffness. Finally, the relation

$$\beta_{tot} \propto P_{in}^{\gamma} \tag{3}$$

determines the energy confinement scaling with power that can be compared with the IPB98(y,2) scaling law, for which $\gamma = 0.31$ [3]. We determine the parameter α by ideal pedestal MHD stability analysis and then we can evaluate γ for various stifness coefficients δ in a self-consistent form and compare to the ITER scaling law value.

The edge MHD stability analysis performed with MISHKA has been carried out for a range of self-consistent plasma equilibria generated with HELENA in which the bootstrap current has been evaluated according to [4] and the pedestal width (in normalized poloidal flux coordinates) has been assumed to be either constant or to scale as $\Delta_\psi \propto \sqrt{\beta_{ped}}$ [5]. The reference pedestal width has been evaluated by application of the model in [6] to ITER plasmas. Our studies have been performed for the flat-top phase of three ITER scenarios (15MA/5.3T Q=10, 10MA/5.3T Q = 5 steady-state and 7.5MA/2.65T half current-half field H-mode scenarios) modelled with ASTRA and CORSICA. MHD stabilty is only evaluated for $s = \sqrt{\psi} \geq 0.5$ as the focus of our study is on the plasma edge.

Results

Figure 1 summarizes the results of the analysis both for constant pedestal width for the 15 MA/5.3 T Q = 10 and the 10 MA/5.3 T steady-state plasma. The stability diagram shows a high β_N limit for both scenarios which corresponds to infernal modes in the core plasma. β_{ped} is limited by external modes which depend on the plasma scenario. For the Q =10 scenario these are the usual peeling-balooning modes with n = 20-30. On the contrary, the steady-state scenario pedestal pressure is limited by low n = 2-4 kink-peeling modes. This difference also modifies the dependence of β_{ped} on β_N which is gradual for the Q = 10 plasma while it is weakly dependent on β_N for wide ranges in this parameter for the steady-state plasma, except at very high β_N values, because of the low n of the instabilities.

The steady state 10 MA case has a much higher stability limit for β_{ped} than the Q = 10 case. This is the result of the lower plasma current and the fact that the stability limit is dictated by kink-peeling modes which scales as $I_p \times B_t$ instead of I_p^2 for ballooning modes.

The points of the upper boundary of stability diagrams have been fitted according to equation 1 to obtain the values of α considering only H-mode conditions ($\beta_N \geq 1.5$ for Q = 10). The results of these fits are shown in figure 2 for the three plasmas studied both considering a constant and varying pedestal width. The 15 MA/5.3 T and 7.5 MA/2.65 T plasmas show similar trends, as expected from balooning stability being dominant, with an increasing β_{ped} with total poloidal β_{tot}. There is no saturation even for β_{tot} values well beyond those required for the achievement of the the Q = 10 goal in ITER at 15 MA ($\beta_{tot} = 0.6 - 0.7$). The values of α (also given in figure 2) for constant pedestal width are much lower than for varying pedestal width showing

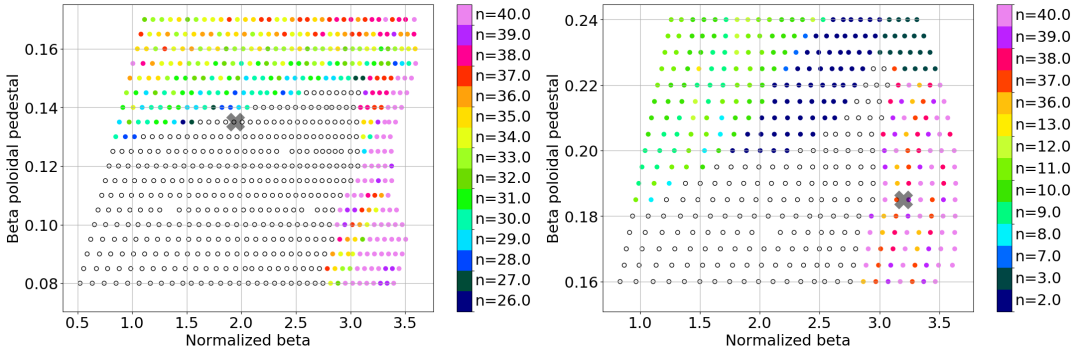

(a) 15MA/5.3T (b) 10MA/5.3T

Figure 1: Edge MHD stability diagram characterized by β_{ped} and β_N for the 15MA/5.3T (left) and 10MA/5.3T (right) plasmas with constant pedestal width. Each point represents a different pressure profile for which stability is calculated for toroidal mode numbers n=[2,40]. The most unstable mode is plotted by color with open circles being stable cases. The reference cases, from ASTRA-CORSICA simulations, are indicated by the black cross.

that the positive feedback between core and edge is increased with the widening of the pedestal at higher pressures. For the 10 MA steady-state case the use of a power law is less suitable due to the different nature of the MHD limit stability. Despite this, the results in 1 show that for this case the results are weakly dependent on the changes of the pedestal width with β_{ped}. In particular for the steady-state Q = 5 reference operating the positive feedback is only significant for $\beta_{tot} > 1.2$ for both cases, which is close to the ITER operational point for this scenario.

The values found for α in these ITER plasmas can be compared to experimental values. From [2], values for α in JET plasmas can be evaluated ($\alpha = 0.41, 0.62$ and 0.79), depending on wall material (C vs. W/Be) and plasma shapes. The case closest to the ITER studies for 15 MA and 7.5 MA plasmas corresponds to the JET high triangularity with the carbon wall; this is also most likely to be the condition in which JET edge stability resembles most that of ITER with high pedestal pressure and high bootstrap current achievable with low gas fuelling.

By assuming values for stiffness, the data from figure 2 can be used to find a value for γ from equation 3. This is done for the 15MA case with varying pedestal width in figure 3. Stiffness values of $\delta = [0.1, 2.0]$ are taken, which then gives a relation between δ and γ:

$$\gamma = 1.18\delta. \tag{4}$$

$\gamma = 0.31$ corresponding to the IPB98(y,2) scaling law requires a stiffness of $\delta = 0.26$ according to our modelling.

Summary

We have applied ideal MHD numerical codes HELENA for equilibrium and MISHKA for edge stability analysis to evaluate self-consistently the MHD stability of a range of ITER plas-

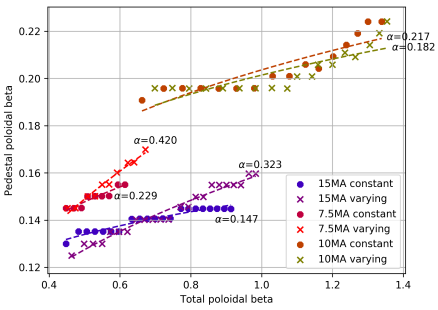

Figure 2: Highest stable β_{ped} values as a function of β_{tot} and corresponding fits for the three ITER plasmas studies, for both constant pedestal width and a pedestal width changing according to the EPED model

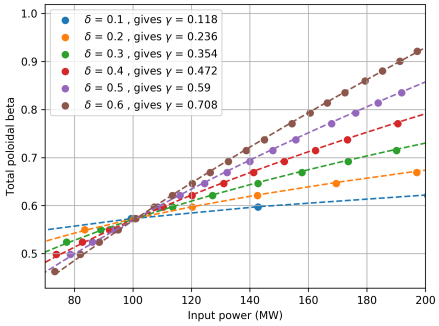

Figure 3: Predicted β_{tot} versus input power for the 15MA plasma with varying pedestal width and β_{ped} limited by edge stability for a range of stiffness parameter δ and resulting energy confinement scaling (γ from equation 3).

mas in terms of the achievable β_{ped} versus β_{tot}. For the 15MA and 7.5 MA plasmas we find that β_{ped} is limited by peeling-balooning modes and increases with β_{tot} according to a power law, whose exponent depends on pedestal width assumptions up to $\beta_{tot} \approx 1$. For the 10 MA steady-state plasmas β_{ped} is limited by low n kin-peeling modes and depends weakly on β_{tot} up to the reference $\beta_{tot} \approx 1.2$. An estimate of the power degradation of energy confinement for a range of core stiffnes parameters for 15 MA plasmas has been provided.

Disclaimer: The views and opinions expressed herein do not necessarily reflect those of the ITER Organization.

ITER is the Nuclear Facility INB no. 174.

References

[1] Wolfrum, E., et al. "Impact of wall materials and seeding gases on the pedestal and on core plasma performance", Nuclear Materials and Energy 12 (2017) 18.

[2] Challis, Clive D., et al. "Improved confinement in JET high ÎŠ plasmas with an ITER-like wall." Nuclear Fusion 55.5 (2015): 053031.

[3] ITER Physics Expert Group on Confinement and Transport et al 1999 Nucl. Fusion 39 2175

[4] Sauter, Olivier, Clemente Angioni, and Y. R. Lin-Liu. "Neoclassical conductivity and bootstrap current formulas for general axisymmetric equilibria and arbitrary collisionality regime." Physics of Plasmas 6.7 (1999): 2834-2839.

[5] Leonard, A. W., et al. "Influence of global beta, shape, and rotation on the H-mode pedestal structure in DIII-D." Physics of Plasmas 15.5 (2008): 056114.

[6] Snyder, P. B., et al. "A first-principles predictive model of the pedestal height and width: development, testing and ITER optimization with the EPED model." Nuclear Fusion 51.10 (2011): 103016.

Appendix C

Input files

C.1 HELENA input file example

Here, an example of a HELENA input file is given. First, some shape parameters are given and the shape is ultimately given by a fourier series (fm(i)). Then the profile parameters are given, and the profiles are given by a number (npts) of datapoints. Finally, physical and numerical parameters are given.

```
 HELENA namelist from EQDSK file (eqdsk2helena)
B(vacuum)   :    5.3000 [T]
current     :   15.0000 [MA]
Rgeo, Zgeo :    6.2149   0.5985 [m]
Rmag, Zmag :    6.3924   0.5985 [m]
q(0)        :    1.0086
p(0)        :    0.8360E+06 [Pa]
 &shape ishape=2, ias=1, mharm=256, xr1 = 0.98, sig1 =0.1,
    imesh=2
     fm(    1)=  0.255460E+01, fm(    2)= -0.000000E+00,
     fm(    3)= -0.782176E-01, fm(    4)= -0.111122E-01,
          ...
     ...
     ...
     fm( 253)= -0.788277E-06, fm( 254)=  0.172089E-05,
     fm( 255)=  0.375688E-05, fm( 256)=  0.496898E-05,
mfm=  256                              &end
 &profile
           igam = 7, ega = 10.0, fga = 1.0, gga=0.01
           ipai = 7, epi = 0.92, fpi = 2.0, gpi=0.04,
                  ICUR=11, DCUR=1.0, ECUR=0.955, FCUR =
                     8.8285293, GCUR=1.0,
                npts =  128, COREP = 1.936, PSIPED = 0.96,
dpr(   1) =  -0.367561E+05, df2(   1) =   0.131333E+02, qin(
   1) =   0.100856E+01, zjz(   1) = 1.0,
dpr(   2) =   0.912921E+05, df2(   2) =   0.637637E+01, qin(
   2) =   0.101804E+01, zjz(   2) = 0.999870720254,
dpr(   3) =   0.131931E+06, df2(   3) =   0.424936E+01, qin(
   3) =   0.102528E+01, zjz(   3) = 0.999484765421,
```

```
...
...
...
dpr(126) =    0.146067E+06, df2(126) =   -0.267300E+01, qin
   (126) =    0.345190E+01, zjz(126) = 0.1440,
dpr(127) =    0.125890E+06, df2(127) =   -0.254721E+01, qin
   (127) =    0.361183E+01, zjz(127) = 0.0752,
dpr(128) =    0.104434E+06, df2(128) =   -0.258045E+01, qin
   (128) =    0.382997E+01, zjz(128) = 0.0,

  &end
  &phys
     eps =    0.318087E+00, alfa =    0.200000E+01, B =
        -0.198464712374, XIAB = 0.179907E+01,
     RVAC =   6.214856, BVAC =   5.300000, BETAP = 0.1,
        BETAP_PED = 0.17,
  &end
  &num nr=201, np=251, nrmap=401, npmap=512,
     nchi=1024, niter=99, nmesh=200,
         NRCUR = 201, NPCUR = 251, ERRCUR = 1.e-5,
  &end
 &pri   npr1 = 1, npr2=1, nrout = 401 &end
  &plot  npl1 = 1 & end
  &ball nqb = 1 &end
```

C.2 MISHKA input file example

A MISHKA input file is given with parameters to start the simulation. However, an elaborate explanation of all parameters is out of the scope of this report.

```
&NEWRUN
  MODE=4, NLTORE = .T., IAS=1
  NG=201,
  IFAST=1,
  RFOUR(1)=-1.,
  VFOUR(1)=-9.,
  q0zyl=-1,
  NTOR = -40,
  VSHIFT(1) = (1.0,0),
  VSHIFT(2) = (0.3,0),
  VSHIFT(3) = (0.1,0),
  VSHIFT(4) = (0.03,0),
  VSHIFT(5) = (0.01,0),
  VSHIFT(6) = (0.003,0),
  VSHIFT(7) = (0.001,0),
  NSHIFT= 7,
  IEQ = 1, DSURF=0., DSURF1=0.,
  ALPHIN = 1.0,
```

```
  SIG1=0.1,
  XR1=0.98,
  RWALL =2.0,     IVAC=1,

  SBEGIN=0.8

  NVPSI = 51, NGV = 51,
  SIGV = 0.1,
&END
&NEWLAN      &END
&NEWRUN   MODE=0 &END
&NEWLAN      &END
```